Study of the Merged Annealing method to establish a reproducible fabrication protocol for perovskite solar cells with competitive efficiencies

Daniel Castillo Bendeck[a,*]

[a]*Department of Chemical Engineering, Universidad de los Andes, Bogotá D.C., Colombia*

Abstract

Perovskite solar cells are growing at an unprecedented rate, so it is important that research groups keep up with state of the art efficiencies to make more relevant contributions. In this work, the *Merged Annealing* method was implemented in search of a reproducible fabrication protocol for high-performing, inverted $MAPbI_3$ perovskite solar cells. It consisted in depositing a PCBM layer on top of the perovskite before its annealing, in order to delay the evaporation of residual precursor solvents. The results showed that this method was able to produce bigger crystals with longer charge-carrier lifetimes compared to the conventional method. This implied better short circuit currents and voltages, and a champion power conversion efficiency of 13.6%. However, it was noticed that the formation of needle-like structures after the *Merged Annealing* was limiting the improvement in efficiency. It was demonstrated that several fabrication parameters were related to this phenomenon, namely the type of substrate, the DMF to DMSO ratio in the precursor solution, the quality of the PCBM layer and the temperature of annealing. By reducing the amount of DMSO, a film without roughness was produced at the expense of smaller crystal sizes, lower efficiencies but fill factors above 80%. Finally, the $MAPbI_3$ solar cells were compared to conventionally annealed $FACsPbI_3$ solar cells, which had a lower band-gap and higher charge-carrier lifetimes. It was observed that the $FACsPbI_3$ perovskite yielded higher short circuit currents, but that the $MAPbI_3$ perovskite deposited through *Merged Annealing* achieved higher fill factors and open circuit voltages.

Keywords:
Perovskite Solar Cell, p-i-n Architecture, $MAPbI_3$, $FACsPbI_3$, Merged Annealing, Solvent Engineering, Parameter Optimization

1. Introduction

Over the last years renewable energies have gained a lot of interest. These new technologies offer an eco-friendly, globally available energy alternative in response to the current global problems regarding climate change, greenhouse gas effects and society's high oil dependence. In fact, they bring other advantages such as the reduction of energetic poverty in non-connected areas, the industrial and technological development around their implementation, the diversification of the energy baskets, and the exploitation of local resources, among others [1]. Within the renewable energies, the solar photovoltaic (PV) systems have grown exponentially. Their production and installation costs have been reduced to the point where, in some countries, they are already cost competitive against fossil-fuel-based technologies [1].

The global power demand projected to the year 2035 is about 20 TW. If it is compared with the 180,000 TW of solar power intercepted by the earth, it is clear that by only harvesting a small fraction of the latter, the world's energy demand could be satisfied [2]. Thus, the photovoltaic systems offer a real solution to the energy problematic, provided that the basic requirements of high efficiency, high lifetime, low costs and low environmental impact are met [3].

The silicon solar cells are nowadays the predominant and most mature photovoltaic technology and have already reached relatively high efficiency values. Their lab record efficiency stands at 26.1% [4] and commercial module efficiencies oscillate between 20% and 22%. Nonetheless, they represent serious problems regarding high production and installation costs and a high carbon footprint [5]. One of the reasons is that silicon has to be melted at very high temperatures to produce the modules. This demands a significant amount of energy that, most often, comes from non-renewable sources. Additionally, this is a thick film technology, which implies that the modules are heavy and rigid and, thus, difficult and expensive to transport and install.

Perovskite Solar Cells (PSC) were introduced in 2009 [8] and have experienced an unprecedented fast growth ever since compared to previous PV technologies. In only 6 years, their record lab efficiency raised from 4% to 21% and the current certified record stands at 24.2% [4]. These cells are based on hybrid metal-organic semiconductor perovskite crystals with a lead halogen frame and small organic/inorganic cations at the interstices. Fig. 1 a) shows a representation of the unitary cell for perovskite crystals. The high performance of these devices has been explained by the excellent optoelectronic properties of this perovskite family, which include a high visible-light absorption efficiency, a tunable direct band-gap, low exciton

☆M.Sc. in Chemical Engineering Thesis.

*Correspondence
Email address: d.castillo1384@uniandes.edu.co (Daniel Castillo Bendeck)

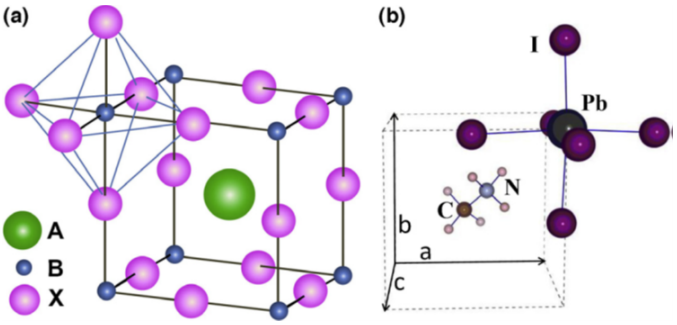

Figure 1: a) Schematic of the unitary cell of a perovskite crystal. A and B are cations and X is an anion. Reprinted from Ref. [6]. b) Schematic of the ion distribution in the $MAPbI_3$ perovskite. Reprinted from Ref. [7].

binding energies, and relatively high electron and hole diffusion lengths [9, 6, 10, 11]. In addition, the perovskites are ionic crystals, which implies that they can be dissolved in organic solvents at ambient temperatures. This allows for the deposition of the perovskite films through ambient temperature solvent methods, making them suitable for low energy, cost effective, high throughput mass production [9]. All these factors, make the PSC technology a strong candidate to replace old PV technology and solve many of the aforementioned problems.

There are two main architectures in PSC: direct and inverted. The difference lies in the direction of electron flow (towards the conductive glass or towards the metal electrode respectively) which is achieved by using different charge-selective layers adjacent to the perovskite. Even though the direct architecture has achieved higher efficiencies, the inverted architecture has gained a lot of attention because of its compatibility with flexible substrates due to low temperature fabrication processes ($< 120°C$) [12], a balanced hole- and electron-transport resulting in hysteresis-less photovoltaic behavior [13], and the possibility of using them in multi-junction solar cells [14].

Initially, the methylammonium lead iodide ($MAPbI_3$) crystal was the most widely used perovskite due to its simple structure and good photovoltaic performance, achieving efficiencies as high as 20% [13, 15, 16]. In Fig. 1 b) its ion distribution can be seen. Nonetheless, it has some disadvantages including a non-optimal bandgap [17], instability induced by temperature and humidity, a structural phase transition at 55°C, and formation of light induced trap-states [18]. To solve these problems, strategies have been proposed to replace the methylammonium (MA^+) cation. For example, a mixture of (MA^+) and formamidinium (FA^+) cations achieved better short circuit currents by lowering the bandgap and taking advantage of a bigger portion of the solar spectrum [17]. Furthermore, the addition of the inorganic metal Cs^+ cation to MA^+FA^+ mixtures enhanced greatly the stability of the films and promoted the crystallization into the photoactive phase [18]. It has also been demonstrated that the MA^+ cation can be completely removed to fabricate $FACsPbI_3$ perovskite solar cells [19].

Most of the significant advancements in PSC have been achieved by an improvement in the photoactive perovskite layer [2]. Early in PSC development, the perovskite was deposited by a simple spin coating and annealing process, but the layers had poor coverage and a highly irregular surface. This was explained by a slow crystallization that allowed the crystals to reorganize and minimize the surface energy [20]. A plethora of methods have been proposed to solve this problem. Some examples are the use of additives in the precursor solution to offer heterogeneous nucleation sites and to promote fast crystallization [21, 13]; the blow of argon during the spin coating to increase the evaporation rate, induce supersaturation and avoid agglomeration [22]; a two-step deposition where the precursors are spin coated sequentially [23, 24]; and, most importantly, what is known as the *Solvent Engineering* method introduced by Jeon et al [25]. The latter consists in the addition of a second solvent (or anti-solvent) to the wet perovskite layer during spin coating that does not dissolve the perovskite, but that is capable of extracting the precursor solution solvents. This induces a fast supersaturation in the wet film and thereby promotes the formation of many nuclei and a subsequent rapid crystallization [2]. A further improvement to the *Solvent Engineering* method was introduced by Anh et al. by using a mixture of dimethylformamide (DMF) and dimethyl sulfoxide (DMSO) as the precursor solution solvent [26]. They demonstrated that the molecules of DMSO form a stable adduct with the PbI_2 and MAI precursors, such that a semi-wet film of this compound is produced after the anti-solvent treatment. It allows for the controlled and reproducible formation of bigger and more uniform crystals during the annealing step, when the DMSO evaporates and the perovskite is formed [26].

Even though these methods are capable of producing very homogeneous films with 100% coverage, they don't ensure that the perovskite will have big crystals with minimized grain boundaries, especially in the vertical direction [27]. The grain boundaries have to be minimized because they offer a higher density of recombination sites, i.e. points in the film where it is much more likely for the charge-carriers to be lost through non-radiative recombination [2]. It has been demonstrated that the ambient temperature, the presence of solvent vapors, differences in heating conditions [18] or the hydrophobicity of the surface below the perovskite [28] can affect the grain size and thus the overall performance. A novel approach to solve this was proposed by Liu et al. in a method they called *Merged Annealing* [27]. It consists in depositing the perovskite through a *Solvent Engineering* method from a DMF:DMSO mixture to obtain the intermediate adduct film. Then, instead of annealing the films to extract the DMSO and form the crystal (*Conventional Annealing*), they first deposit a phenyl$-C_{61}-$butyric acid methyl ester (PCBM) film on top of the $PbI_2 \cdot MAI \cdot DMSO$ adduct and then anneal both films together. According to their study, the PCBM layer blocks the evaporation of the DMSO and forces it to travel sideways to the edges. This has the effect of reshaping the forming perovskite crystals and merging them into bigger crystalline domains. Additionally, it has the effect of improving the contact between the perovskite and PCBM layers because the PCBM molecules can penetrate deeper in the grain boundaries and passivate more defects [27]. Finally, they demonstrated that this method was compatible with different ratios of DMF to DMSO and that it had an effect on the crystallinity and crystal orientation of

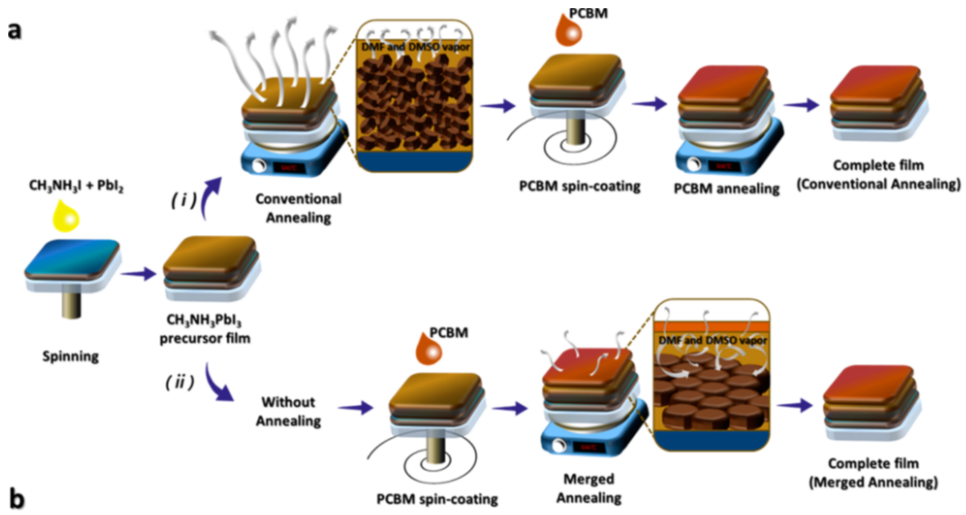

Figure 2: *Merged Annealing* (MA) vs *Conventional Annealing* (CA) methods. The difference is the order in which the perovskite is annealed and the PCBM is deposited. In *Merged Annealing*, the PCBM is deposited first. The resulting crystals are much bigger and uniform. Image reprinted from Ref. [27].

the films [29]. In Fig. 2 a depiction of the *Conventional* and *Merged Annealing* methods is shown.

Throughout the PSC development, it has become clear that reproducing newly reported protocols is not an easy task, partly because of lack of detail in some reported protocols [30] and also because of the unavoidable difference in lab equipment, characterization techniques, conditions, reagents and preparation of the materials, which in perovskites has a tremendous effect [31]. In our research group at the Universidad de los Andes we had been struggling to reach good efficiency values and the reproduction of several conventional protocols was unsuccessful. The objective of this project was to implement the above cited *Merged Annealing* method in our laboratory conditions and understand the effect of several fabrication parameters on the cell performance. The latter, to establish a baseline protocol with an efficiency as high as possible and with high reproducibility. As part of the project, the same protocol was tested at the i-MEET institute at the FAU University in Germany to implement it under strictly controlled conditions. Furthermore, optimized $MAPbI_3$ perovskite layers deposited by *Merged Annealing* were compared with $FACsPbI_3$ perovskite layers deposited by a *Conventional Annealing* method. The architecture of choice for this project was an inverted architecture with the following layers: ITO / PEDOT:PSS / Perovskite / $PC_{61}BM$ / BCP / Ag. Further details concerning each layer will be presented below.

2. Theoretical Framework

2.1. General Solar Cells Working Principle

The photovoltaic energy conversion consists in "the direct production of electrical energy in the form of current and voltage from electromagnetic energy" [3]. The solar cells are the devices capable of such transformation. The following steps are necessary in any solar cell [3]:

1. An incident photon is absorbed in a photoactive material which undergoes an electronic transition from a ground state to an excited state.
2. The excited state is converted into a free negative- and free positive-charge carrier pair.
3. A selective transport mechanism inside the photoactive material drives the positive charge carriers in one direction (towards the anode) and the negative-charge carriers in the other (towards the cathode) where they are collected.
4. The electrons travel through the external circuit doing work and combine with an arriving positive-charge carrier at the anode closing the circuit.

2.2. Inverted Perovskite Solar Cell Working Principle

In Fig. 3 a schematic of the cross section and working principle of an inverted perovskite solar cell is presented. The light comes from the glass side into the perovskite and generates an exciton, i.e. an excited electron and hole pair that is bounded by the electrostatic force (step 1). In these perovskites, the excitons have very low binding energies so that thermal fluctuations are enough to break the bonds and generate free electron and free hole pairs [11] (step 2). These free charge carriers move across the perovskite layer in opposite directions until they meet an adjacent layer that accepts them, driven by the built-in electric field [32] (step 3). For holes, the receiving material is poly(3,4-ethylenedioxythiophene) doped with poly(styrene sulfonate) (PEDOT:PSS), which is a conductive polymer deposited by spin coating from an aqueous suspension. PEDOT:PSS has a highest occupied molecular orbital (HOMO) level slightly above the valence band of the perovskite making the positive-charge transfer energetically favorable, as shown in Fig. 4. The HOMO level for conducting polymers is equivalent to the valence band for semiconductor crystals. For electrons, the receiving material is phenyl$-C_{61}-$butyric acid methyl ester (PCBM), which is a functionalized fullerene, deposited by spin

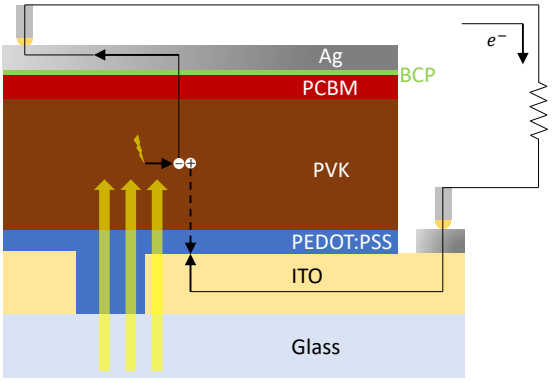

Figure 3: Schematic of the cross section and working principle of an inverted perovskite solar cell. The exciton state is formed somewhere inside the perovskite and spontaneously separates into a free hole and free electron pair. These charge carriers are driven by the built-in field towards opposite electrodes and the electrons travel through the external circuit doing work to recombine with the holes at the ITO anode.

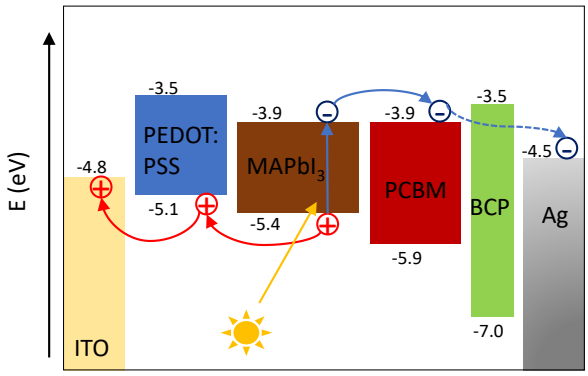

Figure 4: Depiction of the alignment of the energy levels of the layers in Fig. 3. From this figure it is clear that holes and electrons are driven in opposite directions, considering that electrons tend to lower their energy, whereas holes tend to increase it. The energy levels were reproduced from [33, 34].

coating from a chlorobenzene solution. In this case, the conduction band of the perovskite is perfectly aligned with the lowest unoccupied molecular orbital (LUMO) level of PCBM, so that the negative charge transfer is possible as depicted in Fig. 4. In this case, the LUMO level is equivalent to the conduction band. Both PEDOT:PSS and PCBM are selective contacts because the transfer of the other charge-carrier would require additional energy.

While the holes are transferred directly from PEDOT:PSS to the transparent indium tin oxide (ITO) anode, the electrons tunnel through a $\sim$ 5nm nonconductive bathocuproine (BCP) layer to reach the silver (Ag) cathode. The reason for this, is that the contact between the PCBM and Ag layers is not ohmic but forms a Schottky junction, which hinders the electron transfer [35]. The BCP avoids this and the electrons easily tunnel through the thin BCP layer. Finally, the electrons travel through the external circuit doing work and recombine with the holes at the anode (step 4).

2.3. JV curves and theoretical model

Given the inherent variability in solar intensity, researchers have established standard solar spectra to be able to make comparisons between devices. The most common in PSC (and the one used in this project) is the AM1.5G, which has an integrated power density of 100mW/cm^2.

The most direct way of testing solar cell performance is through the measurement of the current as a function of the applied voltage under standard solar irradiance. An important procedure is to normalize the current by the photoactive area of the device, in order to be able to compare devices with different areas. This normalized current is denoted as the current density J and has units of $[\text{mA/cm}^2]$. The resulting graph is called a JV-curve and many important performance parameters can be extracted from it.

Fig. 5 shows in blue a real JV curve obtained in this project. By convention, the positive currents are in the direction of photogeneration. This means that the first quadrant displays the power generation zone. The generated power density is calculated by:

$$P = J \times V \tag{1}$$

In Fig. 5 this quantity is plotted in orange and it can be seen that there is a maximum power (mp) point. The corresponding voltage and current density values are denoted by V_{mp} and J_{mp} respectively. The power conversion efficiency (PCE) is defined as the maximum generated power density divided by the incoming standard power density:

$$\text{PCE} = \frac{P_{mp}}{P_{in}} = \frac{P_{mp}}{100\text{mW/cm}^2} = \frac{J_{mp} \times V_{mp}}{100\text{mW/cm}^2}, \tag{2}$$

The maximum theoretical efficiency of a solar cell is a function of the bandgap of the photoactive layer. It can be demonstrated by thermodynamic considerations that the maximum achievable efficiency is around 33% for a bandgap of 1.4 eV [36, 37]. For $MAPbI_3$ perovskites, with a bandgap close to 1.5 eV, the maximum achievable efficiency is 31.6% [38].

Other important parameters that can be extracted from the JV curves are the short circuit current density J_{sc} and the open circuit voltage V_{oc}. The former is the maximum current density that the cell is capable of producing, when there is no external resistance and the terminals are short-circuited. In this case, the built-in field is the highest and most of the excited charges are collected. As the external resistance is increased, a voltage is forced between the electrodes, that starts to counterbalance the internal field. When the external resistance becomes infinite, the voltage between the terminals is maximum and there is no current flow since the built-in field is completely counterbalanced. The voltage at this point is the V_{oc}. Both quantities are pointed out in Fig. 5. The maximum theoretical values for 1.5 eV bandgap materials are $28.97\,\text{mA/cm}^2$ and $1.215\,\text{V}$ respectively [38].

Finally, a measure of the ideality of the cell is given by the fill factor (FF), which is defined by:

$$FF = \frac{P_{mp}}{J_{sc}V_{oc}} = \frac{J_{mp}V_{mp}}{J_{sc}V_{oc}} \tag{3}$$

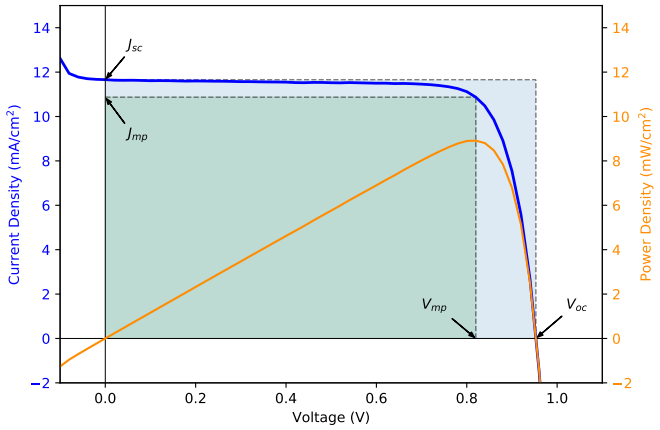

Figure 5: In blue, JV curve of a real device from this project. In orange, the corresponding PV curve. The short circuit and maximum point current densities as well as the open circuit and maximum point voltages are pointed out. The ratio of the area of the colored rectangles is equal to the fill factor.

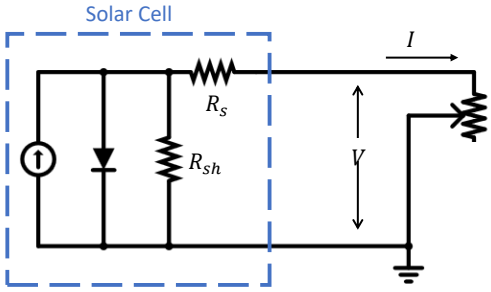

Figure 6: Equivalent circuit model of a solar cell inside the blue box. The external variable resistor is shown, which determines the operating voltage and current.

This quantity relates the real maximum power with the power that could be achieved if all short circuit electrons were delivered at open circuit voltages. Not even the ideal cells achieve this because of radiative recombination, but they set an upper limit of 89.9% for 1.5 eV bandgap materials [38]. Interestingly, there is a graphical interpretation of the FF and it can be seen in Fig. 5. The numerator in equation 3 is the area enclosed by the green rectangle, while the denominator is the area enclosed by the blue rectangle. The FF is the ratio between these areas, i.e. the percentage of area that the green rectangle is able to cover from the blue rectangle.

The J_{sc}, V_{oc} and FF quantities are directly related to the PCE, as can be seen if we combine equations 2 and 3 to obtain:

$$\text{PCE} = \frac{J_{sc} \times V_c \times FF}{100\text{mW/cm}^2}, \tag{4}$$

Which shows that to achieve a good efficiency it is necessary to improve independently each of these three parameters.

A simple and fundamental way of modeling a solar cell is by the superposition of a current source and a diode in parallel. This comes from the fact that a solar cell is approximately a rectifying diode with a big contact area. Moreover, to take into account non-idealities, a series resistance R_s and a shunt R_{sh} can be added to the model. In Fig. 6 the graphical representation of this model is presented. Ideally, the R_{sh} should be as high as possible to avoid current leakages. The source of a low R_{sh} is mainly attributed to fabrication defects in the films that represent direct paths between electrodes. The presence of a low shunt resistance causes a steep slope at the short circuit condition in a JV curve (but is not the only cause) [39].

On the other hand, R_s should be as small as possible, to avoid resistive power losses. Contributors to the R_s are the intrinsic bulk resistances of the solar cells materials, the bulk resistances of metal contacts and interconnections and the contact resistance between metallic contacts and the semiconductors in the cell. The presence of a high series resistance causes a less pronounced slope at the open circuit condition (but is not the only cause) [39].

One way of estimating these resistances is by performing dark JV measurements. In the model this is equivalent to setting a null current for the current source. As a very good approximation, especially for small values, R_{sh} can be estimated by measuring the inverse of the slope at the short circuit condition. Additionally, R_s can be approximated as the inverse of the slope at high applied voltages, when the curve becomes linear instead of exponential. At this voltage regime, the diode has an effective resistance close to zero and R_s dominates. These estimations can also be performed on JV-curves of illuminated devices, but they are less accurate because changes in slope can also come from phenomena related to the non-equilibrium condition.

3. Methodology

As described above, the experiments were run at two different laboratories with some important differences. From now on, the conditions at Uniandes will be referred to as *Conditions A* and the conditions at i-MEET will be referred to as *Conditions B*.

3.1. Baseline Device Fabrication Protocol

The baseline Fabrication Protocol will be described under *Conditions A*.

3.1.1. ITO substrate cleaning and activation

A depiction of the patterned ITO (Kintec, 15 Ω/□) is shown in Fig. 7 (a), with 2 x 1.5 cm dimensions. Neutral laboratory detergent was diluted in water in a 1:50 vol. proportion and the substrates were softly brushed with the detergent solution for 10 seconds. Then, they were sonicated in detergent water for 20 minutes. Meanwhile, deionized (DI) water was heated to the boiling point in a crystallizer glass. The sonicated substrates were immersed in the boiling water and then, were further cleaned with copious amounts of running DI water. After this, the substrates were sonicated for 10 minutes in DI water and finally rinsed with running DI water. Finally, the glasses were put on a heating plate at 150 °C for about 10 minutes until completely dry.

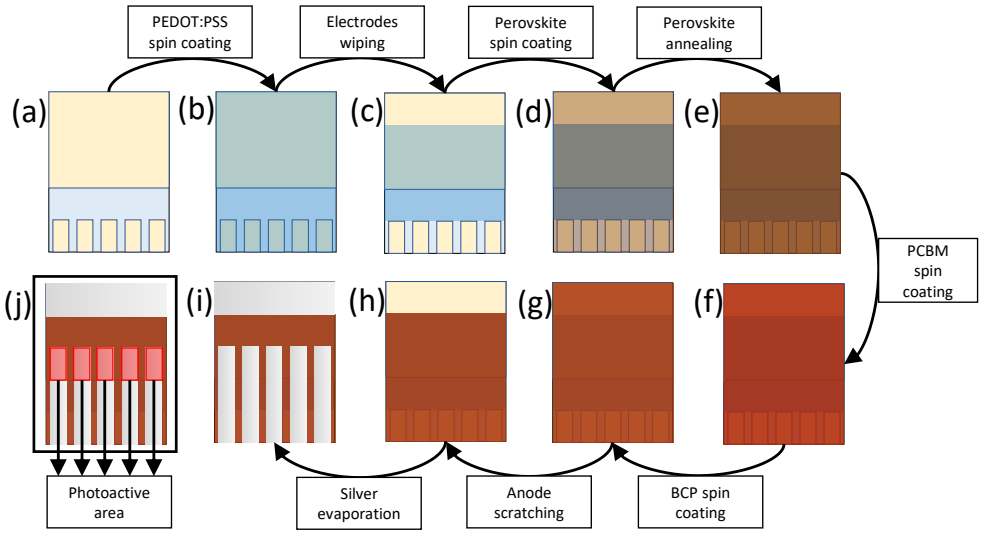

Figure 7: Schematic of the fabrication procedure for an inverted PSC. a) Depiction of the patterned ITO substrate used in *Conditions A*. In yellow the conducting ITO and in clear blue the glass. b) PEDOT:PSS layer. c) Wiping of PEDOT:PSS at the electrodes. d) $PbI_2 \cdot MAI \cdot DMSO$ adduct before annealing. e) Annealed Perovskite layer. f) PCBM layer. g) BCP layer. h) Scratching of the anode with a razor blade. i) Evaporation of silver. j) Estimated photoactive area from the intersection of the Ag pixels and the ITO anode.

Right before the PEDOT:PSS deposition, the glasses were transferred to a glass tray and put inside an air plasma cleaner (Harrick PDC-32G) for 15 minutes to further clean them and also activate the surface and enhance its hidrophilicity.

3.1.2. PEDOT:PSS deposition

The PEDOT:PSS (Ossila, Al4083, 1.3-1.7%wt. in water) suspension was filtered through a 0.45 µm PVDF filter and was diluted with 10% vol. ethanol. All cleaned substrates and the PEDOT:PSS suspension were transferred to a dry air glovebox with humidity below 20%. The spin coating rotation was set to 8000 rpm and after blowing the substrate, the rotation was initiated and 35 µL of the PEDOT:PSS suspension were dispensed on the substrate. After spinning for 40 s, a wet cotton swab was used to remove the PEDOT:PSS layers from both electrodes to avoid short-circuiting the pixels at the cathode and to improve contact at the anode. Then, the films were annealed at 150 °C for 20 minutes ((a) to (c) in Fig. 7).

3.1.3. Solutions preparation

A (nominal) 1.2M $MAPbI_3$ perovskite solution was prepared inside a dry air glovebox according to the following parameters. For 1 mL of solution, 1.2 moles of PbI_2 (Aldrich, 99%) and MAI (GreatCell Solar) were weighted in separate vials. A 1:9 vol. mixture of DMSO and DMF (Panreac 99.5 and 99.8% respectively) was prepared and 1 mL of it was poured on the PbI_2 vial. It was heated to 180 °C and stirred at 500 rpm to accelerate dissolution. When the PbI_2 was totally dissolved, the vial was left to cool to ambient temperature and then, the contents were poured on the MAI vial. After mixing well and making sure that all MAI was dissolved, the contents were poured back to the PbI_2 vial. This ensured a slight PbI_2 excess. The solution was immediately used.

The PCBM solution was prepared by adding 1 mL of chlorobenzene to 20 mg of PCBM (1-Material >99%) and stirring overnight at 500 rpm and 70°C. Finally, the BCP solution was prepared by mixing methanol and toluene in a 1:10 ratio and preparing with it a 5 mg/mL solution of BCP. Then, 0.1 mL of this concentrated solution were diluted with 0.9 mL of methanol to produce a final 0.5 mg/mL BCP solution.

3.1.4. Solar cell fabrication

The solar cells were manufactured inside a glove box with constant N_2 flow of 10 L/min. This ensured a relative humidity below 5% and an oxygen content below 5% vol. 30 µL of the perovskite solution were spread on the PEDOT:PSS layer and the substrate was spun at 5000 rpm for 10 s. 150 uL of chlorobenzene were dispensed with a micropipette 5 s after the start of the spinning. The films were annealed for 20 minutes at 100 °C on a hot plate. Then, the PCBM solution was heated to 40°C and 20 µL of it were dispensed dynamically by spin coating on the perovskite layers at 3000 rpm. On top of it, 35 µL of the BCP solution were deposited at 4000 rpm. Next, a razor blade was used to remove the layers on top of the ITO anode. Finally, the silver contacts were thermally evaporated at a rate of 0.2 Å/s during the first 5 nm and at 1 Å/s until 100 nm ((c) to (i) in Fig. 7). The photoactive area was estimated as the intersection between the ITO and Ag electrodes, which approximately has an area of 8 mm^2. It is shown in red in Fig. 7 (j) for all 5 pixels.

The latter was the procedure for the *Conventional Annealing* method. For the *Merged Annealing* method, the PCBM was spin coated before annealing the perovskite, as shown in Fig. 2.

3.1.5. Changes in Conditions B

The process under conditions B was very similar, but there were some important modifications that need to be mentioned.

Table 1: Summary of the different experimental conditions at Uniandes and i-MEET.

Variable	**Conditions A**	**Conditions B**
Laboratory	Uniandes	i-MEET
Glovebox O_2 levels	< 5% vol.	< 10 ppm
Glovebox H_2O levels	< 5% RH	< 1 ppm
PbI_2 purity	> 99%	> 99.9985%
Filtered perovskite and PCBM solutions	No	Yes
ITO sheet resistance and dimensions	(15 Ω/□), 2×1.5 cm^2, 5 pixels	(10 Ω/□), 2.5×2.5 cm^2, 6 pixels
Substrate cleaning procedure	Detergent - DI Water	Detergent - DI Water - Acetone - Isopropanol
PEDOT:PSS spin coating method	Dynamic, 10% ethanol, inside glovebox	Static, not diluted, outside glovebox
Evaporator	outside glovebox	inside glovebox

First, the PbI_2 had a much higher purity (Alpha, 99.9985%). The BCP and MAI were exactly the same, the PEDOT:PSS was nominally the same but was bought from Heraeus and the PCBM was bought from Solene with the same purity. Secondly, the glovebox conditions were much more controlled, having always a concentration of water and oxygen below 1 and 10 ppm respectively. Third, all solutions were filtered either with PA or PTFE filters right before the deposition. Fourth, the ITO substrates (10 Ω/□) were bigger, 2.5x2.5cm, had 6 pixels and a different layout. Fifth, the substrates were further cleaned with acetone and isopropanol after the detergent solution. Sixth, the PEDOT:PSS layer was deposited outside the glovebox with a different procedure because the one used in *Conditions A* didn't produce good films at *Conditions B*. It consisted in activating the substrates under UV/ozone for 10 minutes and applying 100 µL of undiluted PEDOT:PSS suspension on the ITO before initiating rotation. Then, accelerating to 4500 rpm and letting rotate for 40 s. Finally, the silver evaporator was inside the glovebox under *Conditions B*, such that the films were never exposed to the atmosphere before evaporating. Table 1 summarizes this differences for quick reference.

3.1.6. FACsPbI$_3$ film fabrication

In this case, FAI (GreatCell Solar), CsI (Sigma, 99.999%) and PbI_2 (Alpha, 99.9985%) were weighted in the same vial, to prepare a 1.4M $FA_{0.85}Cs_{0.15}PbI_3$ solution in a 4:1 DMF to DMSO ratio with a 1% PbI_2 excess. The solution was stirred at 70°C overnight and it was filtered with a PTFE filter. 50µL of the perovskite solution were dispensed on top of the PEDOT:PSS layer. Then, the following spin coating program was started: 3s at 200 rpm, 5s at 2000 rpm and 40s at 5000 rpm. At the 20th second of the last step, 200 µL of CB were added with the micro-pipette. Then, the substrates were conventionally annealed at 100°C for 20 minutes.

3.2. Characterization methods

The cells fabricated in each of the laboratories were characterized using different equipment:

3.2.1. Conditions A

JV curves were measured under simulated AM 1.5G light (100 mW/cm^2) from a solar simulator Abet Technologies model 10500 sweeping from -0.1 to 1.1 V at 50 mV/s with an Autolab AUT84194 potentiostat. The photoactive area was exactly measured by taking a picture of the cell and correcting the perspective to measure the area of the intersection between the ITO and Ag electrodes using the ImageJ software. For the stability studies, the samples were measured at atmospheric conditions (~70% RH) but they were stored in a dark nitrogen atmosphere.

SEM images were taken with a Tescan Lyra 3 microscope. The average perovskite grain size was roughly estimated by the line intercept method, by which a line of known distance L is drawn on the SEM image and the number of crossed grain boundaries N_{GB} is counted. The average grain size is then approximately given by:

$$\langle D \rangle = L/N_{GB} \tag{5}$$

3.2.2. Conditions B

JV curves were measured under simulated AM 1.5G light (100 mW/cm^2) from an Oriel Sol1A solar simulator calibrated with a Newport standard silicon solar cell. The voltage sweep was conducted from -0.1 to 1.1 V at 100 mV/s with a Keithley 7013-S source. The photoactive area was determined in a similar way as in *Conditions A*. Profilometry analysis was done with a Tencor profilemeter. SEM images were taken with a Jeol 7610-F microscope. Transient photo-luminescence spectra were taken with a Fluotime 300 from Picoquant. UV vis spectra were measured with a Perkin Elmer Lambda 950 equipment. Finally external quantum efficiency (EQE) was measured with a Enlitech QE-R3011 device. This quantity is calculated as a function of wavelength and is given by:

$$EQE = \frac{\text{number of photon incident on active area}}{\text{number of electrons produced}} \tag{6}$$

The EQE spectrum can be integrated along with the theoretical MA1.5G spectrum to determine the expected J_{sc} value and compare it to the JV curve measurement.

The stability measurements were performed inside a LED illuminated chamber with approximately 1 sun intensity. The atmosphere of the chamber was constantly refreshed with new N_2 and the cells were cooled down with a fan cooling system to a working temperature of 25°C.

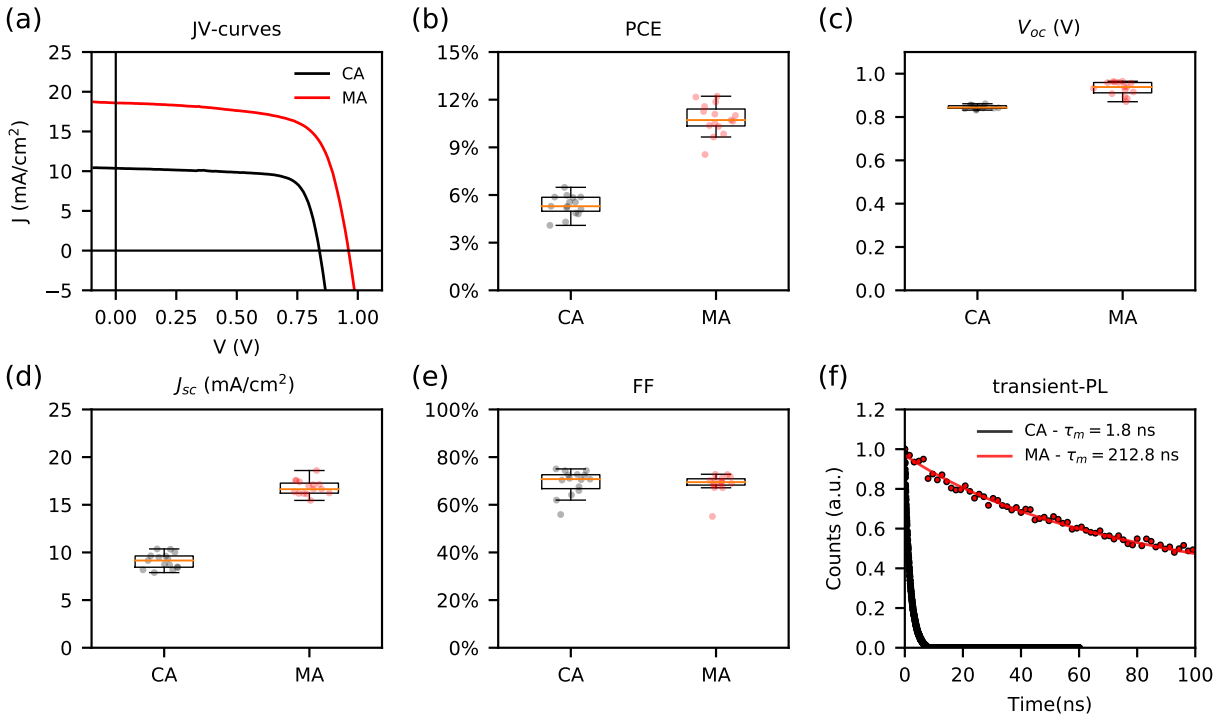

Figure 8: Comparison of *Conventional Annealing* (CA) vs *Merged Annealing* (MA) methods for $MAPbI_3$ perovskite solar cells fabricated under *Conditions A*. (a) JV curves for the best pixels of each variation under exactly the same experimental conditions. (b)-(e) Box and whisker plots of the performance parameters for each variation are shown superimposed on the data: (b) power conversion efficiency (PCE), (c) open circuit voltage (V_{oc}), (d) short circuit current (J_{sc}) and (e) fill factor (FF). (f) Transient photoluminescence results for CA and MA perovskites deposited on glass substrates. The intensity weighted mean lifetime is displayed for each variation as τ_m. The adjusted model was a biexponential curve.

4. Results and Discussion

4.1. Merged Annealing for $MAPbI_3$ perovskite solar cells

Conventional vs Merged Annealing

Preliminary work under *Conditions A* had shown that the implementation of the *Conventional Annealing* method (from now on CA) could produce cells with decent V_{oc} and high FF, but there was a serious problem regarding the short circuit currents. For example, in figure A1 it can be seen that regardless of the variation of ethanol percentage in the PEDOT:PSS suspension, the currents were very low with respect to the theoretical maximum and also with respect to the literature reported values (20-25 mA/cm^2). This lead us to the implementation of the *Merged Annealing* method (from now on MA) that enhanced the perovskite layer quality dramatically.

Fig. 8 (a) shows the champion JV curves for the CA and MA methods in an experimental run where everything else was identical. In this experiment, 3 cell replicates were made with each method and each cell had 5 pixels, for a total of 15 (semi-independent) samples. Figs. 8 (b)-(e) display the different parameters extracted from the JV curves. It is clear that the MA cells had a significantly superior performance. The main difference lay in the higher J_{sc} values for MA, that implied an almost doubled PCE. Regarding the V_{oc} and FF, the effect was less important. Incidentally, this particular run for CA had relatively low V_{oc} values but other CA experiments achieved comparable values to the MA method, for example in Fig. A1. It is interesting to note, that the FF already had competitive values, but the highest efficiency achieved in this run was of 12.2%, way lower than the champion efficiency of 18.3% reported by Liu et al. in the original *Merged Annealing* article [27]. The reason is that they obtained higher FF values and current densities above 20 mA/cm^2.

The thicknesses of the perovskite films resulting from CA and MA were found to be almost the same by profilometry analysis. Under the basic conditions reported in the methodology section, the thicknesses were around 320 nm. This makes sense, given the fact that the adduct film is already formed with a particular thickness and what changes is the way the residual DMSO is evaporated. The fact that MA produced cells with much higher J_{sc} than CA, shows that the problem with CA was not one of photon absorption but one of charge collection.

A transient photo-luminescence analysis was performed on CA and MA perovskite samples deposited on glass to determine effects on mean charge-carrier lifetimes. The results are shown in Fig. 8 (f). Here, it can be seen that the lifetime of the MA sample is more than 200 times higher than the one for the CA sample. This can be associated with better crystal quality and a lower density of traps in the MA samples. Thus, the JV results could be explained by a higher trap density for the CA samples. In particular, it can be argued that the traps in this case are deep, such that even at short circuit conditions the built-in field is not able to extract the charges that fall on them. The ones that

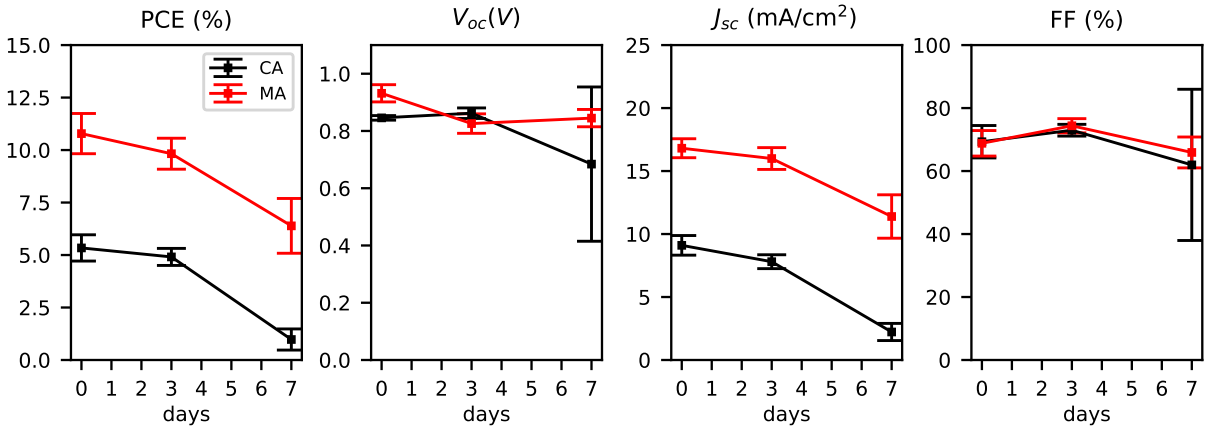

Figure 9: Stability study for CA vs MA cells fabricated under *Conditions A* in terms of power conversion efficiency (PCE), open circuit voltage (V_{oc}), short circuit current (J_{sc}) and fill factor (FF). The points are mean values and the error bars are one standard deviation in each direction.

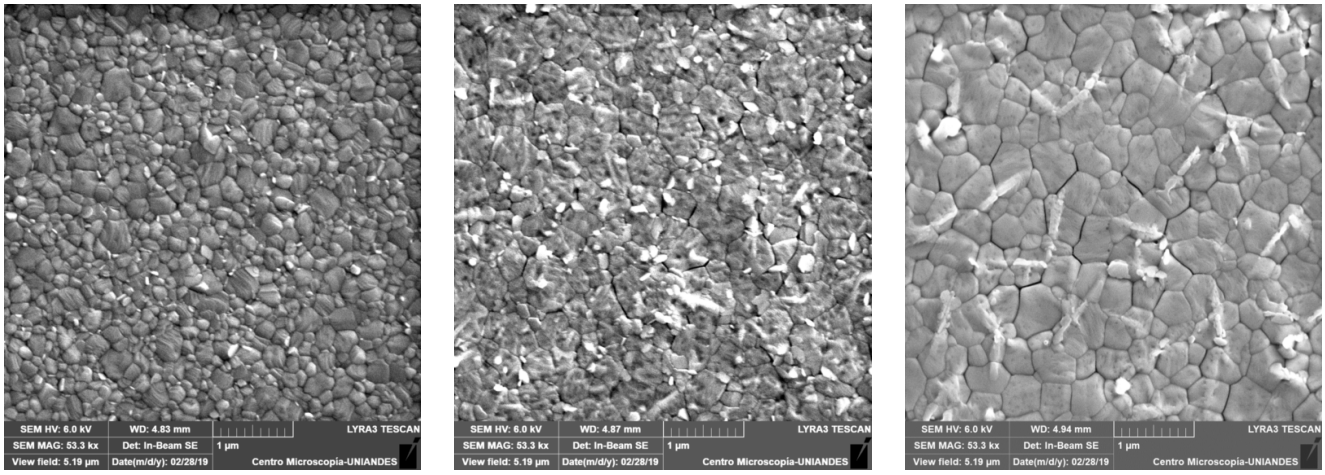

(a) CA - $\langle D \rangle$ = 150 nm (b) MA - PCBM @ 3000 rpm $\langle D \rangle$ = 350 nm (c) MA - PCBM @ 1500 rpm $\langle D \rangle$ = 300 nm

Figure 10: SEM frontal images of $MAPbI_3$ perovskites deposited using CA and MA under *Conditions A*. For MA two different depositions speeds for PCBM were used, 3000 and 1500 rpm. The latter had a thicker PCBM film. Before observation, the PCBM was washed away with chlorobenzene. $\langle D \rangle$ means average grain size, estimated by the line intercept method.

don't fall would be efficiently extracted independently of the applied field, explaining thus the good FF with low J_{sc} for the CA method [16].

A stability study was conducted on these samples that is shown in Fig. 9. The first observation is that in both cases the cells are very unstable, especially for CA. While the CA cells were almost dead after 7 days, the MA cells retained about 50% of the original efficiency after the same time on average. From this figure, it is also clear that the major cause of efficiency loss is a significant drop of J_{sc} in time. Notably the rate at which the J_{sc} drops for each method is very similar in absolute terms. This, along with the fact that the FF is more or less constant, hints that the degradation mechanism is such, that the loss in J_{sc} could be explained mainly by a steady increase in deep traps, as discussed above. On the other hand, the V_{oc} values display an initial drop to a value slightly above 0.8 V but then remain more or less constant. Interestingly, the FF experiences a raise after three days and then slowly goes back to the original value. The low stability of these devices has been reported before and has been explained by the acidic and hydrophilic nature of PEDOT:PSS that easily reacts with the perovskite [34] and frees volatile species containing iodine (for example MAI) that eventually react with the Ag electrode forming AgI [40].

To check the effect of MA on crystal growth, frontal SEM pictures of $MAPbI_3$ perovskites deposited on PEDOT:PSS by both methods were taken (Fig. 10). For MA, a variation in the deposition speed of PCBM was conducted (3000 vs 1500 rpm) to have different PCBM thicknesses. The first observation is that the crystals in CA are significantly smaller than for both MA cases. The mean crystal size for each case was estimated with the line intercept method using equation (5). The approximate values were 150 nm for CA, 350 nm for MA with 3000 rpm PCBM and 300 nm for MA with 1500 rpm PCBM. It is important to notice that the thickness of the PCBM layer had a sig-

nificant impact on the crystals for the MA route. Even though in both cases the crystals are bigger than in CA, the crystals of the 1500 rpm variation are more defined and there is a presence of needle-like structures on top of the crystals. The 3000 rpm variation is more irregular at the surface but the crystals are bigger by more than 50 nm on average. Given that a thicker film is less likely to have pinholes or cracks and, thus, it confines better the DMSO vapors, this difference hints that the rate at which the DMSO vapors escape through the PCBM is a key parameter. The effect of the PCBM thickness was also tested in JV-curves, shown in Fig. A2 C and D. The 3000 rpm variation displayed a slightly better performance, mainly because of higher J_{sc} values.

The SEM images explained why the MA films had much higher lifetimes than the CA films. The crystal sizes were on average significantly higher for MA and, in many cases, they were bigger than the average film thickness. This implied that the amount of grain boundaries was greatly reduced. The traps and recombination centers are more likely to form at the boundaries, so they were also reduced. With such crystal sizes, it is expected that the carriers only have to transverse one crystal in the vertical direction, making the probabilities of extraction much higher and achieving higher J_{sc} values.

Surface roughness and needle-like structures

Despite the big jump in performance thanks to the MA route, it still needed to be improved to reach efficiencies close to the ones reported in the literature. One possible reason for the poorer performance of these devices was that a significant roughness developed on the perovskite layer after the *Merged Annealing*. This phenomenon was not observed in the CA samples nor is it reported in the original paper [27]. Moreover, it was noticed that the roughness was not always the same, even for replicate samples. Some would be more dark and shiny and others would be greyer and with micro-artifacts already noticeable by looking at the films. The samples in Fig. 10 were relatively smooth, but there were other more extreme cases, where optical microscopy revealed that the roughness came from the presence of needle-like structures with lengths in the tens of microns, as is shown in Fig. 11. There was a hidden variable that was not being taken into account and this led to an exhaustive study of the different MA parameters. Some of the most interesting experiments are summarized in table 2 along with the respective references to the supporting data in the appendix.

While optimizing the annealing temperature, it was remarkable that the lowest temperature (80°C) yielded cells that were not rough at all, and yet their performance was very bad, probably because there was still DMSO inside the film. Nonetheless, it is important to notice the effect of annealing temperature on the formation of the rough surfaces. The champion efficiency of this project was obtained in this batch of cells, with a value of 13.6% for the 100°C + 20 minutes variation, as can be seen in Fig. A3 F. Here, J_{sc} values above 20 mA^2/cm and record voltages above 1V were achieved. Furthermore, the reproducibility within and between cells was remarkable. However, the perovskites were still very rough and the FF wasn't very good, mainly because the JV curve had a steep slope at the short circuit condition. To try to understand the cause of this, R_{sh} values were estimated from the JV curves both at illuminated and dark conditions. The results, shown in Fig. 12, demonstrate that the problem was not one of shunting paths because the estimated dark shunt resistances were much higher than the ones under light. This means that, most likely, the steep slope in the JV curve was caused by shallow traps in the perovskite layer that are easily avoided by the charge-carriers at short circuit conditions, given the strong built-in field. However, as soon as the external voltage raises and counterbalances the built-in field, more and more charge-carriers get trapped and the current drops quickly [16]. This means that there is still room for improvement in the crystal quality, perhaps by increasing even more the crystal sizes and/or reducing the roughness.

An interesting result was obtained in an experiment where the intermediate adduct went through a 30s CA at different temperatures before coating with PCBM and performing the MA. The idea was to remove excess DMSO and, thus, try to reduce the roughness. The results can be seen in Fig. A6. As expected, the higher the temperature of the intermediate CA step, the darker the films were before MA and the less rough they were after it. However, the results showed that, even though the roughness disappeared, the JV performance dropped with the

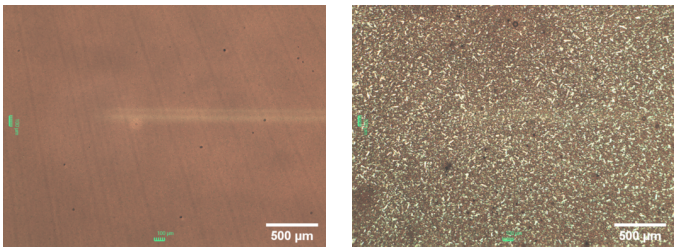

(a) CA (b) MA

Figure 11: Optical microscopy images of $MAPbI_3$ perovskite films deposited by (a) CA and (b) MA. The latter was rinsed with chlorobenzene to remove the PCBM.

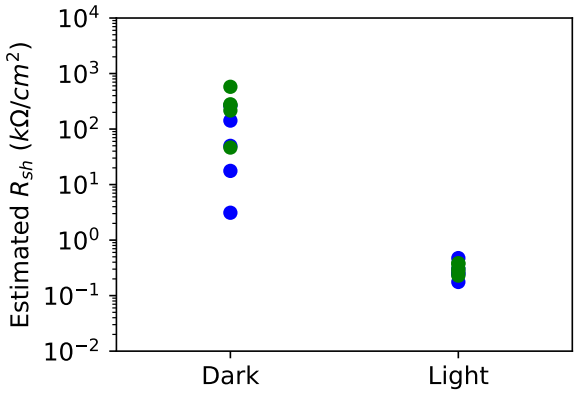

Figure 12: Shunt resistance estimation of a MA $MAPbI_3$ PSC, whose JV curve presented a steep slope at the short circuit condition under illumination. Estimated as the inverse of the slope at short circuit conditions both under 1 sun illumination (Light) and in the dark. Dots of the same color represent pixels of the same solar cell.

Table 2: Summary of several experiments to optimize the MA route under *Conditions A*. If not explicitly stated, the conditions for all other parameters were the same as described in the methodology section.

Variable	Levels studied	Observations and recommendations	Evidence
Time of CB addition	5, 6 [s]	Both yielded similar values, the addition window is thus at least between the 5th and the 6th seconds.	Fig. A2 B vs C
PCBM rpm (thickness)	1500, 2000, 3000, 4000 [rpm]	In general, a higher speed (lower thickness) yielded higher J_{sc}. The effect on FF depended on the roughness of the perovskite. In one run there was no improvement in FF by using 1500 rpm over 3000 rpm. In another run, 4000 rpm yielded higher J_{sc} but lower FF than 2000 rpm. Recommendation: make the PCBM as thin as the perovskite underneath allows. The roughness decreased slightly for lower thicknesses.	Fig. A2 C vs D Fig. A5
Annealing Temperature	80, 90, 100, 105, 110 [°C]	There is clearly an optimum of efficiency around 100 and 105°C. Both lower and higher values show decreased FF and V_{oc}. The lower temperatures yielded films without roughness but it seems that there was still DMSO inside because performance was very bad.	Figs. A3 and A4
Annealing time	10, 20, 30 [min]	The longer the better, at least until 30 min. However, the differences between 10 and 20 are more pronounced than between 20 and 30 min. All are rough.	Figs. A3 and A4
PbI_2 to MAI molar ratio	1.05 : 1, 1 : 1, 1 : 1.05	PbI_2 excess seems to yield the best results, improves both V_{oc} and J_{sc}. Molar ratio seems to have an effect on FF that is dependent on the PCBM thickness. The PbI_2 excess also helped reducing the roughness significantly.	Fig. A5
Intermediate - CA Temperature	40,60,80,100 [°C]	This factor refers to the temperature at which some perovskite layers were CA treated during 30s before the PCBM deposition and MA. The higher the temperature, the darker the film, the less DMSO before MA and the less rough the film at the end. However, the best result was obtained with 40°C, which yielded cells that were still very rough. By taking out the DMSO, the needles disappear but also the desired effect is lost.	Fig. A6

temperature. The optimum of efficiency was found for a temperature of 40°C, at which the cells were just a bit less rough than the ones without this intermediate step. Basically, removing DMSO before MA hinders the formation of roughness, but at the same time hinders the desired effect of crystal growth and merging. Therefore, a different MA strategy has to be found that achieves big crystals but at the same time doesn't induce the formation of needle-like structures.

Surface Roughness under Conditions B

Under *Conditions B*, an important observation was that the MA films could be made always shiny if deposited on PEDOT:PSS with a DMF to DMSO ratio of 10:1 instead of 9:1. However, when the substrate was changed to ITO, or when the DMSO amount was increased, the films looked rougher and similar to the ones obtained under *Conditions A*. Fig. 13 shows a comparison of pictures and SEM images of MA perovskite layers deposited under *Conditions B* either on PEDOT:PSS or on ITO. The film on PEDOT:PSS is very uniform, doesn't have surface artifacts, as compared to the ones in Fig. 10 (b) and (c) and has an average crystal size of 240 nm. This might be related to the higher purity of PbI_2 and the more controlled atmosphere conditions. On the other hand, the sample deposited on ITO has very big crystals with diameters in the order of micrometers intercalated with long branched structures. These structures were already observed at the beginning of PSC development when no *Solvent Engineering* techniques were available and the crystals grew in an uncontrolled manner minimizing surface area [20]. Despite the big crystals, this kind of film is undesirable for solar cells because the coverage is poor and also because the branched structures can penetrate the PCBM and get in direct contact with the silver electrode.

Both the PEDOT:PSS and ITO substrates have very low roughnesses. Therefore the difference in crystal structure has

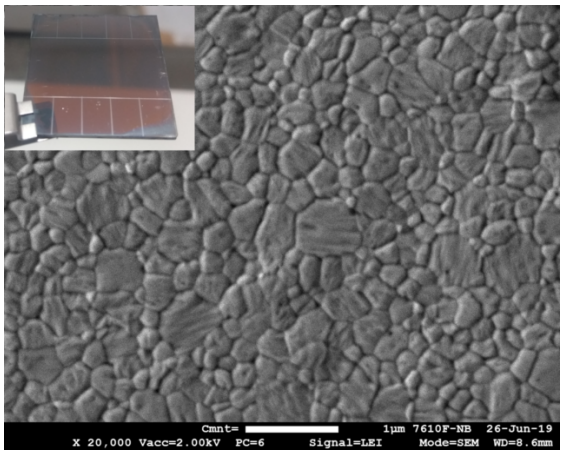

(a) MA on PEDOT:PSS - $\langle D \rangle$ = 240 nm

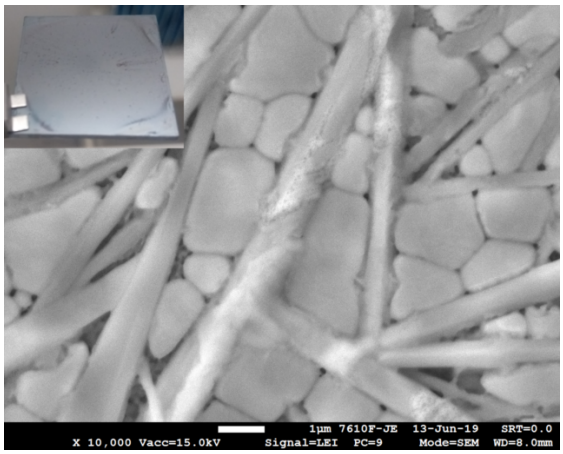

(b) MA on ITO - $\langle D \rangle$ > 1000 nm

Figure 13: SEM frontal images of $MAPbI_3$ perovskites deposited by MA on PEDOT:PSS or ITO under *Conditions B* and a DMF to DMSO ratio of 10:1 vol. Note that the magnifications are different. The scale bar is equal to 1 µm. The insets show photographs of the observed layers. Before observation, the PCBM was washed away with chlorobenzene. $\langle D \rangle$ means average grain size, estimated by the line intercept method.

more to do with the interaction energy between the perovskite and the surface on which it forms. In this case, PEDOT:PSS is much hydrophilic than ITO and Bi et al. demonstrated that this has an important effect on the crystal growth since more hydrophilicity means more heterogeneous nucleation points and a slow down of the grain boundary displacement [28].

These results show that the surface on which the perovskite grows is critical in determining the final crystal properties. In fact, a different brand of ITO substrates was also tested under *Conditions B* to fabricate exactly the same solar cells, but the resulting perovskite films on PEDOT:PSS displayed roughness and the solar cells had a poorer performance. The comparison of the JV curves is shown in Fig. A7 between graphs B and H. This shows that even for substrates of the same material, small differences can lead to strong effects on crystal growth, so that the optimization has to be different for each laboratory and substrate type.

It was also observed that by increasing the amount of DMSO in the precursor solution, the films were rougher. However, SEM images revealed that in this case the roughness was caused by a different kind of structure, as can be seen in Fig. A9 for a perovskite deposited from a 4:1 DMF to DMSO precursor solution. Here, the crystals are bigger than 1µm and aggregate in clusters, leaving void spaces. The corresponding JV performance was comparable to the 10:1 version as can be seen in Fig. A7 by comparing graphs B and G.

The cell fabrication under *Conditions B* implied new challenges. For instance, the cells were much more sensitive to the chlorobenzene (CB) anti-solvent treatment, in particular to the time of CB addition and its volume. This can be seen in Fig. A7 comparing A, B and C for the former and D, B and E for the latter. It was found that it was better to add the CB at the 6th second and using at least 300 µL of CB, instead of the 150 µL needed under *Conditions A*. This might be due to the extremely dry environment in which the cells were produced. Some works [41, 15] have highlighted the role of H_2O molecules in the formation of perovskite and how they have a competing effect with DMSO. Thus, the change in atmosphere conditions requires a whole new optimization.

As a general observation, the currents obtained under *Conditions B* were lower than those obtained under *Conditions A*, but the FF were higher. This probably stems from the difference in crystals obtained from MA at each set of conditions (compare Fig. 10 (b) with Fig. 13 (a)). Under *Conditions B*, the crystals were smaller than the film thickness on average, implying that the amount of grain boundaries that the charge-carriers had to transverse was higher, and thus the obtained currents lower. However, the better coverage and uniformity and probably the higher chemical purity helped to obtain better fill factors. A compromise between reproducibility, high FF, medium V_{oc} and medium J_{sc} was achieved with a perovskite deposited by a two-step spin coating program (10s at 1000 rpm and then 10s at 5000 rpm), adding 300 mL of CB at the 5th second and depositing the PCBM at 2000 rpm. The corresponding JV curves are presented in Fig. A8 C. Even though for this variation the currents were relatively low, the fill factors were reproducibly very high, in some cases even above 80%. The two-steps spin coating method yields an approximately 50% thicker film (~ 450 nm), which might be the main cause for the improvements in FF and reproducibility.

A very interesting result was obtained during the optimization experiments for *Conditions B*. In an experiment with twelve similar cells, almost all performed badly and only one performed very well. Fig. 14 (a) shows in blue a pixel of the special cell, against one"identical" replicate in green. The only apparent difference between the one that performed well and the others was that for this particular cell, accidentally 2 small drops of CB were added instead of one big drop. The adduct film looked darker after this accident and the resulting cell was much better. This shows that not only the time of addition and the volume of CB are important, but also the way in which it is added has a significant impact. To understand the cause of this

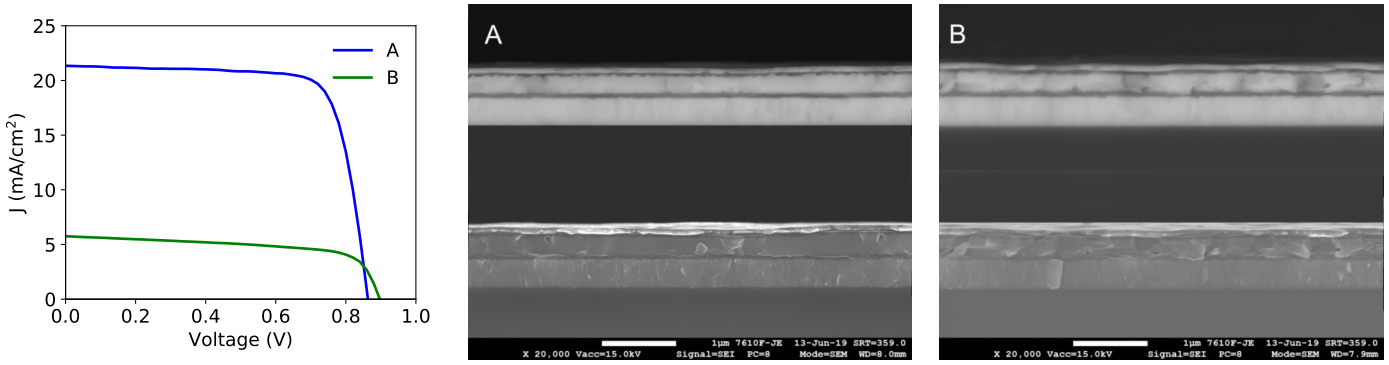

(a) (b) (c)

Figure 14: (a) JV curves of $MAPbI_3$ PSC fabricated with MA under exactly the same conditions, except that the chlorobenzene was dispensed in two drops instead of one for the blue curve - A. In this experiment, the perovskite was 1.0M in concentration, therefore the films look relatively thin. (b) Cross sectional SEM images of a cell with good performance (blue in (a)). (c) Cross sectional SEMs image of a cell with bad performance (green in (a)). A retro-dispersed electrons image is presented above and a secondary electrons image is presented below.

big difference, cross-section SEM images were taken both of the well-performing cell and of a badly performing one. They can be seen in Fig. 14 (b) and (c) respectively. The difference is pretty clear. While the perovskite in the well-performing cell had very big crystals and few grain boundaries and defects, the badly performing one had a much more disorganized crystal structure, a lot of grain boundaries and small crystals. This proved that the MA route can produce very good films but that the external parameters have to be controlled very strictly because small changes can lead to bad films.

To summarize, these results showed that the perovskite growth under the MA route is very sensitive to the following factors:

- DMSO evaporation rate and path: the more confined the DMSO, the rougher the cells.
- Amount of DMSO in the precursor solution: the less DMSO content, the less rough but also the smaller the crystals.
- Annealing temperature: the lower the temperature, the less rough the films.
- Interaction with substrate: the more hydrophobic the substrate, the rougher and the bigger the crystals.

A procedure that allows to have bigger crystals without the formation of the needle-like structures and that is less sensitive to small changes in the fabrication procedures, especially in very dry atmospheres, is yet to be found. A hint in this direction is the low roughness for low annealing temperatures. Perhaps a gradual increase in the annealing temperature can induce a more controlled growth of big crystals and the disappearance of the needle-like structures.

4.2. $FACsPbI_3$ perovskite solar cells

In addition to the *Merged Annealed* $MAPbI_3$ (MA-$MAPbI_3$) perovskite solar cells, conventionally annealed $FACsPbI_3$ (CA-$FACsPbI_3$) perovskite solar cells were fabricated under *Conditions B* following the same architecture. The protocol for this perovskite used a DMF to DMSO ratio of 4:1. The full details are given in the methodology section. It is important to mention, that these films were thicker ($\sim$ 630 nm) because the concentration of the perovskite was 1.4M.

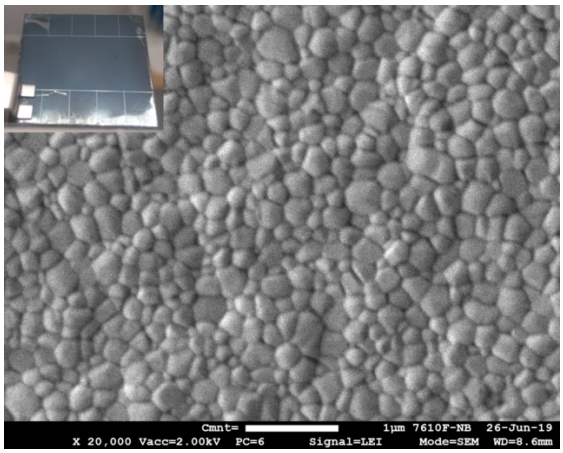

Figure 15: CA-$FACsPbI_3$ perovskite on PEDOT:PSS - $\langle D \rangle$ = 200 nm. $\langle D \rangle$ means average grain size, estimated by the line intercept method.

Fig. 15 shows the SEM image of a $FACsPbI_3$ film deposited on PEDOT:PSS. It can be seen that the crystals have an estimated mean size of 200 nm, a value between the mean sizes for CA-$MAPbI_3$ and MA-$MAPbI_3$. In this case, films deposited on PEDOT:PSS and on ITO looked almost identical, which was also confirmed by UV-vis. Therefore, this perovskite protocol was less sensitive to the interaction energy with the substrate. Note that given the mean crystal size of 200 nm and the layer thickness of $\sim$ 630 nm, one should expect on average three crystal layers in the vertical direction.

A study of the CB addition time (18, 20 and 22s) was performed for this route, which can be seen in Figs. A8 D-F. The first observation is that the results are very grouped and that all three addition times yield similar results. As the time of addition is increased, J_{sc} is slightly reduced but its dispersion is also reduced. A compromise was made by selecting the 20s varia-

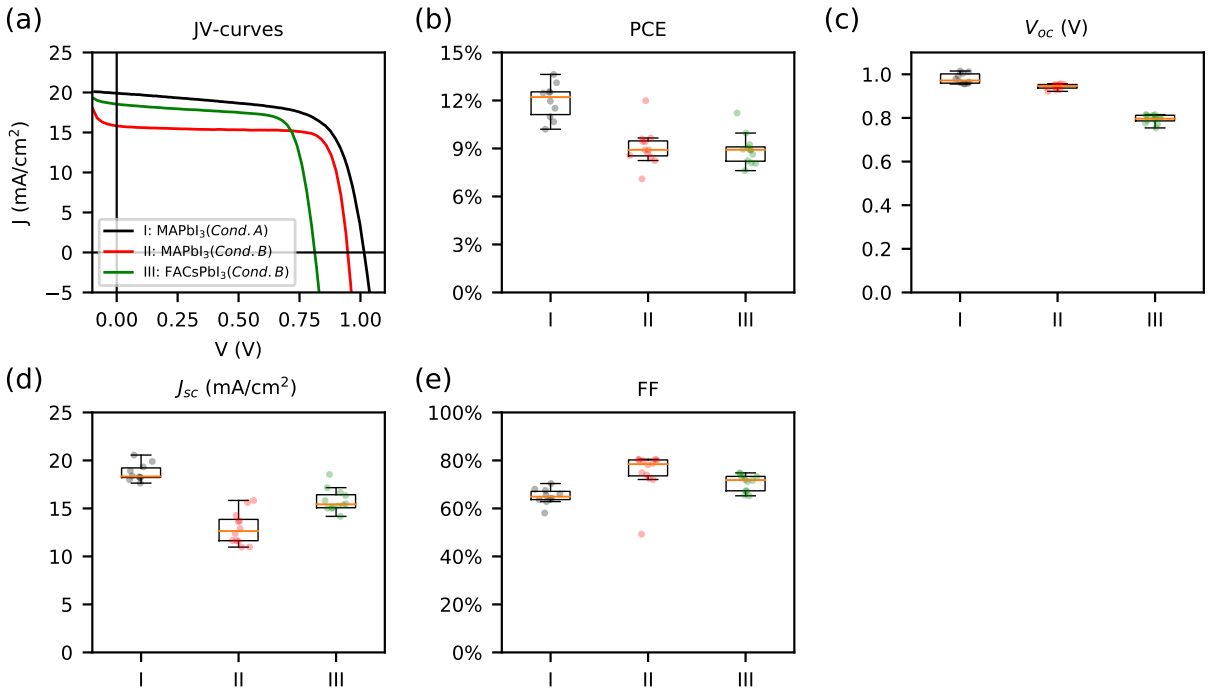

Figure 16: Comparison between MA-$MAPbI_3$ and CA-$FACsPbI_3$ cells. I: $MAPbI_3$ cells fabricated under *Conditions A* with the MA route. II: most reproducible and FF record $MAPbI_3$ cells fabricated under *Conditions B* with the MA route. III: $FACsPbI_3$ cells fabricated under *Conditions B* with the CA route. (a) JV curves for the best pixels of each variation. (b)-(e) Box and whisker plots of the performance parameters for each variation are shown superimposed on the data: (b) power conversion efficiency (PCE), (c) open circuit voltage (V_{oc}), (d) short circuit current (J_{sc}) and (e) fill factor (FF)

tion for the comparison with the $MAPbI_3$ perovskites. Comparing this study with the CB addition time (4, 5 and 6s) study for MA-$MAPbI_3$ perovksites in Figs. A7 A-C it can be seen that the operating window for the $FACsPbI_3$ route is bigger, making the deposition method more robust. One of the reasons is that this route has a higher amount of DMSO, which has a lower vapor pressure than DMF and delays the evaporation process of the intermediate film.

Fig. 16 shows a comparison between MA-$MAPbI_3$ cells fabricated under *Conditions A*, MA-$MAPbI_3$ cells fabricated under *Conditions B* and of CA-$FACsPbI_3$ cells fabricated under *Conditions B*. For the MA-$MAPbI_3$ cells fabricated under *Conditions B* the two-step spin coating variation was selected, which did not have the champion pixel in terms of efficiency, but which had the best reproducibility between and within experiments and had the FF record. It is very interesting that even though under *Conditions A* the atmosphere was not as controlled and the PbI_2 was not as pure as under *Conditions B*, the best performance in terms of PCE, V_{oc} and J_{sc} was obtained under the former. Only FF was better for the MA-$MAPbI_3$ fabricated under *Conditions B*. This definitely had to do with the time that was available for optimization in both places, and highlights the variability in results between different laboratories. Comparing only the cells fabricated under *Conditions B*, it can be seen that the MA method for $MAPbI_3$ achieved better FF and V_{oc} than the CA method for $FACsPbI_3$. However, the $FACsPbI_3$ cells had on average higher J_{sc} values. This suggests testing in the future the MA method in $FACsPbI_3$ cells to get the best out of the two methods.

To further understand the differences between these perovskites, several physical properties were compared under *Conditions B* and are shown in Fig. 17. The dark JV curve estimation of the series resistance in Fig. 17 (a) shows that both perovskites offer more or less the same bulk resistance. On the other hand, the dark JV curve estimation of the shunt resistance in Fig. 17 (b) shows that there is a big dispersion in the data but that the MA-$MAPbI_3$ films yield higher R_{sh} on average, which partly explains the higher FF for this variation. Regarding the transient PL plots in Fig. 17 (c) the behaviour is quite interesting because the CA-$FACsPbI_3$ sample has a quicker drop at the beginning, but then it stabilizes and actually achieves a mean charge-carrier lifetime higher than the one for the MA-$MAPbI_3$ sample. This evidences two facts. First, that probably the main recombination mechanisms are different in each layer and second, that for $FACsPbI_3$ the crystal size is not as important to achieve higher charge-carrier lifetimes as is the case for $MAPbI_3$ (See Fig. 8 (f)). This explains the relatively high currents in spite of having three grain boundaries in the vertical direction on average.

The UV-vis spectra in Fig. 17 (d) show that the absorption is higher in the $FACsPbI_3$ sample, mainly because it is thicker and also that $FACsPbI_3$ has a lower bandagap. Fig. 17 (e) shows the external quantum efficiency (EQE) of cells with the different perovskites. In both cases, the EQE is relatively low throughout the spectrum, which explains the low J_{sc} values obtained under *Conditions B*. In both cases, the integrated J_{sc} value was very

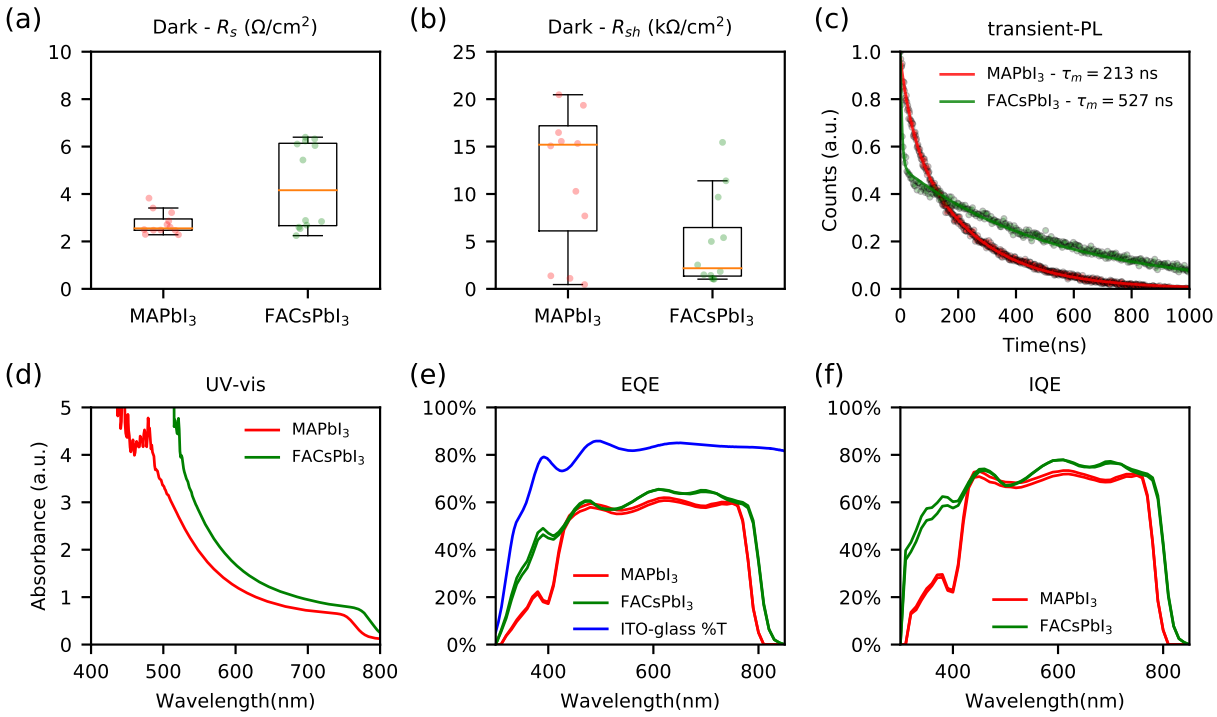

Figure 17: Comparison between MA-MAPbI$_3$ and CA-FACsPbI$_3$ perovskites fabricated under *Conditions B*. (a) R_s estimated values from dark JV curves of cells fabricated with these layers. (b) R_{sh} estimated values from dark JV curves of cells fabricated with these layers. (c) Transient photoluminescence results for MAPbI$_3$ and FACsPbI$_3$ perovskites deposited on glass substrates. The intensity weighted mean lifetime is displayed for each variation as τ_m. The adjusted model was a biexponential curve. (d) UV-vis spectra for both perovskites. (e) External quantum efficiency (EQE) spectra for cells fabricated with both perovskites. Each has a replicate. Also shown is the transmission spectra of the ITO substrate used to calculate the internal quantum efficiency (IQE) spectra in (f).

close to the measured value in JV-curves. To establish if the problem was one of absorption or charge collection, the transmission spectrum of the ITO-glass was measured (also shown in Fig. 17 (e)) and it was used to make a rough estimate of the internal quantum efficiency (IQE), i.e. the ratio of generated electrons per photon absorbed. The estimated IQE spectra are shown in Fig. 17 (f). On the one hand, it is clear that the ITO glasses don't have a very high transmission and are a clear source of lost photons (either absorbed or reflected). However, the IQE shows that more than 20% of the excited charge carriers are lost internally through recombination mechanisms. Finally the QE graphs show that the increase in current for the FACsPbI$_3$ is mainly due to the smaller bandgap that redshifts the QE curve.

A stability study under inert atmosphere and constant 1 sun illumination was conducted to compare the MA-MAPbI$_3$ and CA-FACsPbI$_3$ cells fabricated under *Conditions B*. The results for 6 days of measurements are shown in Fig. 18, where the results are normalized to the value in the first measurement. The non-normalized results are shown in Fig. A10. One interesting observation is that, even though some pixels of the MA-MAPbI$_3$ cells started to show contact problems after some time, the CA-FACsPbI$_3$ were much more robust and the contacts remained intact in almost all pixels. This could be associated with the greater thickness and also the smaller densely packed crystals. Regarding the PCE, it can be seen that in both cases it drops approximately at the same rate and that the cells are not very stable. As with the cells fabricated under *Conditions A* in Fig. 9, the V_{oc} was more or less constant but a very interesting phenomenon happened here with J_{sc} and FF. Within the first few hours, the currents started to get bigger with time, achieving values 50% higher than the initial ones, especially for MAPbI$_3$. However, the improvement in current density for MAPbI$_3$ came with a corresponding decrease in FF, mainly because of an ever increasing (absolute) slope at the short circuit conditions until the FF reached values below 30%. This suggests a light induced change that was not observed in the samples fabricated under *Conditions A*. Conversely, the FF values of the FACsPbI$_3$ cells were more stable and some retained the initial value.

5. Conclusions

The *Merged Annealing* method was implemented under two different laboratory conditions to fabricate MAPbI$_3$ perovskite solar cells. It was demonstrated that it had a positive impact in crystal size and charge-carrier lifetimes, that implied better short circuit currents and open circuit voltages compared to the *Conventional Annealing* method. A 13.6% champion efficiency was obtained at Uniandes after several optimization experiments.

It was observed that after the *Merged Annealing* process a roughness developed on the perovskite films due to the uncontrolled growth of the crystals into needle -like structures inter-

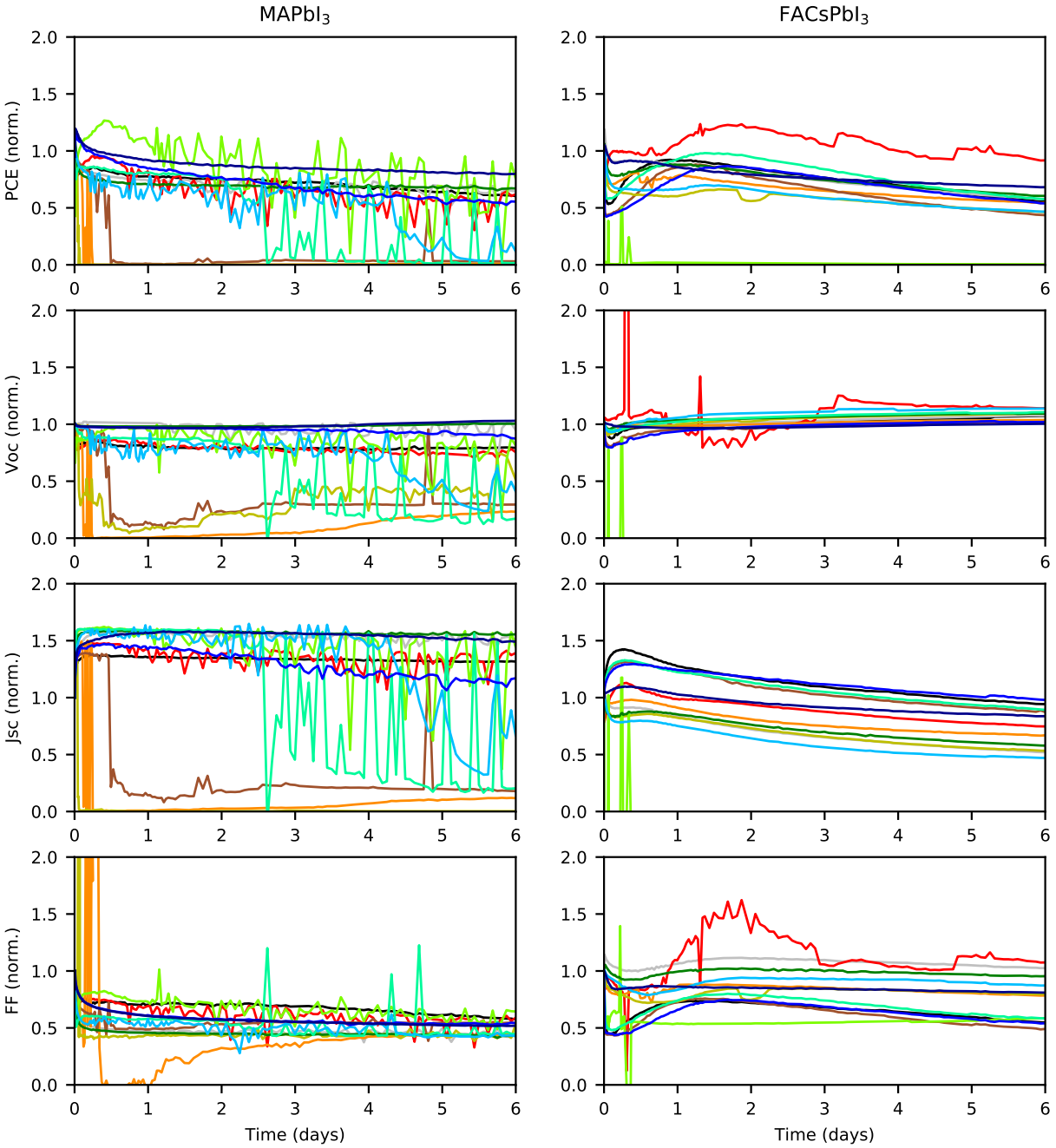

Figure 18: Stability study for the different perovskite solar cells fabricated under *Conditions B*. The cells were constantly kept under constant 1 sun illumination, constant 25°C temperature and inert atmosphere. The values are normalized to the initial value.

calated with big crystals. This is thought to be one of the efficiency limiting factors. Several experiments demonstrated that this phenomenon and the crystal size were affected by the quality of the PCBM layer, the temperature of annealing, the DMSO content and the interaction with the substrate. It will be interesting to explore in the future the possibility of gradually increasing the annealing temperature to have a more controlled growth and remove the needle-like structures. This would allow to use a higher DMSO amount and a more hydrophobic substrate to increase the crystal size.

In addition, it was determined that the *Merged Annealing* method is very sensitive to the laboratory conditions and that the procedures have to be reoptimized for each lab and substrate conditions. Under more strictly controlled atmosphere conditions and with a higher purity PbI_2, the surface roughness was eliminated by using a 10:1 DMF to DMSO precursor solution instead of 9:1. The crystal sizes decreased and with them the PCE and J_{sc} values, but the better coverage and uniformity achieved FF values above 80%.

$FACsPbI_3$ perovskite solar cells were also fabricated with a *Conventional Annealing* procedure and were compared to the *Merged Annealed* $MAPbI_3$ devices. The results showed that *Merged Annealing* was capable of producing higher FF and V_{oc} but that the *Conventional Annealing* $FACsPbI_3$ cells could achieve higher currents on average. It was demonstrated that the shunt resistances were higher for *Merged Annealing* $MAPbI_3$ cells, partly explaining the FF improvement. Conversely, the smaller bandgap of *Conventional Annealing* $FACsPbI_3$ and the higher lifetimes explain the improvement in J_{sc} for the latter. Both devices displayed low EQE, both because of a low transmission of the ITO substrates but also because of internal recombination.

Finally, stability studies showed that this architecture is very unstable and many efforts have to be put into achieving longer lifetimes for the devices. In particular, the *Conventional Annealing* $FACsPbI_3$ showed a better FF stability and better electrical contact. Future work should be directed towards the implementation of the *Merged Annealing* method in the $FACsPbI_3$ perovskites to get the best out of both.

Acknowledgement

I acknowledge the financial support from the Chemical Engineering Department at Universidad de los Andes, from the i-MEET Chair at the Friedrich Alexander Universität, and from the German Academic Exchange Service DAAD. The latter provided the full financial support for the short-term stay at i-MEET.

Also, I thank my mentor, professor Pablo Ortiz, for his support and advice throughout the project. Additionally, I thank professors María Teresa Cortés and Christoph Brabec for their advice and for sharing their lab equipment for this project, Eider Erazo and Martín Gómez for their invaluable help in the lab and Thomas Heumüller for his good advice and support. Finally, I thank my father, my mother, Lala and Mari, whose support was key for the successful completion of this project.

References

[1] REN21, Renewables 2017 Global Status Report, 2017.

[2] S. D. Stranks, P. K. Nayak, W. Zhang, T. Stergiopoulos, H. J. Snaith, Formation of Thin Films of Organic–Inorganic Perovskites for High-Efficiency Solar Cells, Angewandte Chemie International Edition 54 (2015) 3240–3248.

[3] S. J. Fonash, Solar Cell Device Physics, 2nd ed ed., Academic Press/Elsevier, Burlington, MA, 2010.

[4] NREL, Best Research-Cell Efficiencies, https://www.nrel.gov/pv/assets/pdfs/best-research-cell-efficiencies-190416.pdf, 2019.

[5] P. V. Kamat, Meeting the Clean Energy Demand: Nanostructure Architectures for Solar Energy Conversion, The Journal of Physical Chemistry C 111 (2007) 2834–2860.

[6] N.-G. Park, Perovskite solar cells an emerging photovoltaic technology, Materials today 18 (2015) 65–72.

[7] G. Giorgi, J.-I. Fujisawa, H. Segawa, K. Yamashita, Small Photocarrier Effective Masses Featuring Ambipolar Transport in Methylammonium Lead Iodide Perovskite: A Density Functional Analysis, The Journal of Physical Chemistry Letters 4 (2013) 4213–4216.

[8] A. Kojima, K. Teshima, Y. Shirai, T. Miyasaka, Organometal Halide Perovskites as Visible-Light Sensitizers for Photovoltaic Cells, Journal of the American Chemical Society 131 (2009) 6050–6051.

[9] F. X. Xie, D. Zhang, H. Su, X. Ren, K. S. Wong, M. Graetzel, W. C. Choy, Vacuum-assisted thermal annealing of CH3NH3PbI3 for highly stable and efficient perovskite solar cells, ACS nano 9 (2015) 639–646.

[10] J. M. Ball, M. M. Lee, A. Hey, H. J. Snaith, Low-temperature processed meso-superstructured to thin-film perovskite solar cells, Energy & Environmental Science 6 (2013) 1739–1743.

[11] J. Boucl'e, N. Herlin-Boime, The benefits of graphene for hybrid perovskite solar cells, Synthetic Metals 222 (2016) 3–16.

[12] J. You, Z. Hong, Y. Yang, Q. Chen, M. Cai, T.-B. Song, C.-C. Chen, S. Lu, Y. Liu, H. Zhou, et al., Low-temperature solution-processed perovskite solar cells with high efficiency and flexibility, ACS nano 8 (2014) 1674–1680.

[13] J. H. Heo, H. J. Han, D. Kim, T. K. Ahn, S. H. Im, Hysteresis-less inverted ceCH3NH3PbI3 planar perovskite hybrid solar cells with 18.1% power conversion efficiency, Energy & Environmental Science 8 (2015) 1602–1608.

[14] K. A. Bush, A. F. Palmstrom, J. Y. Zhengshan, M. Boccard, R. Cheacharoen, J. P. Mailoa, D. P. McMeekin, R. L. Hoye, C. D. Bailie, T. Leijtens, et al., 23.6%-efficient monolithic perovskitesilicon tandem solar cells with improved stability, Nature Energy 2 (2017) 17009.

[15] C.-H. Chiang, M. Khaja Nazeeruddin, M. Grätzel, C.-G. Wu, The synergistic effect of H 2 O and DMF towards stable and 20% efficiency inverted perovskite solar cells, Energy & Environmental Science 10 (2017) 808–817.

[16] Y. Ma, Y. Liu, I. Shin, I.-W. Hwang, Y. K. Jung, J. H. Jeong, S. H. Park, K. H. Kim, Understanding and Tailoring Grain Growth of Lead-Halide Perovskite for Solar Cell Application, ACS Applied Materials & Interfaces 9 (2017) 33925–33933.

[17] N. Pellet, P. Gao, G. Gregori, T.-Y. Yang, M. K. Nazeeruddin, J. Maier, M. Grätzel, Mixed-Organic-Cation Perovskite Photovoltaics for Enhanced Solar-Light Harvesting, Angewandte Chemie International Edition 53 (2014) 3151–3157.

[18] M. Saliba, T. Matsui, J.-Y. Seo, K. Domanski, J.-P. Correa-Baena, M. Khaja Nazeeruddin, S. M. Zakeeruddin, W. Tress, A. Abate, A. Hagfeldt, M. Grätzel, Cesium-containing triple cation perovskite solar cells: Improved stability, reproducibility and high efficiency, Energy & Environmental Science 9 (2016) 1989–1997.

[19] Y. Yu, C. Wang, C. R. Grice, N. Shrestha, J. Chen, D. Zhao, W. Liao, A. J. Cimaroli, P. J. Roland, R. J. Ellingson, Y. Yan, Improving the Performance of Formamidinium and Cesium Lead Triiodide Perovskite Solar Cells using Lead Thiocyanate Additives, ChemSusChem 9 (2016) 3288–3297.

[20] G. E. Eperon, V. M. Burlakov, P. Docampo, A. Goriely, H. J. Snaith, Morphological Control for High Performance, Solution-Processed Planar Heterojunction Perovskite Solar Cells, Advanced Functional Materials 24 (2014) 151–157.

[21] Y.-J. Jeon, S. Lee, R. Kang, J.-E. Kim, J.-S. Yeo, S.-H. Lee, S.-S. Kim,

J.-M. Yun, D.-Y. Kim, Planar heterojunction perovskite solar cells with superior reproducibility, Scientific Reports 4 (2014).
[22] F. Huang, Y. Dkhissi, W. Huang, M. Xiao, I. Benesperi, S. Rubanov, Y. Zhu, X. Lin, L. Jiang, Y. Zhou, A. Gray-Weale, J. Etheridge, C. R. McNeill, R. A. Caruso, U. Bach, L. Spiccia, Y.-B. Cheng, Gas-assisted preparation of lead iodide perovskite films consisting of a monolayer of single crystalline grains for high efficiency planar solar cells, Nano Energy 10 (2014) 10–18.
[23] Z. Xiao, C. Bi, Y. Shao, Q. Dong, Q. Wang, Y. Yuan, C. Wang, Y. Gao, J. Huang, Efficient, high yield perovskite photovoltaic devices grown by interdiffusion of solution-processed precursor stacking layers, Energy & Environmental Science 7 (2014) 2619–2623.
[24] C.-H. Chiang, Z.-L. Tseng, C.-G. Wu, Planar heterojunction perovskite/PC 71 BM solar cells with enhanced open-circuit voltage via a (2/1)-step spin-coating process, Journal of Materials Chemistry A 2 (2014) 15897–15903.
[25] N. J. Jeon, J. H. Noh, Y. C. Kim, W. S. Yang, S. Ryu, S. I. Seok, Solvent engineering for high-performance inorganic–organic hybrid perovskite solar cells, Nature Materials 13 (2014) nmat4014.
[26] N. Ahn, D.-Y. Son, I.-H. Jang, S. M. Kang, M. Choi, N.-G. Park, Highly reproducible perovskite solar cells with average efficiency of 18.3% and best efficiency of 19.7% fabricated via Lewis base adduct of lead (II) iodide, Journal of the American Chemical Society 137 (2015) 8696–8699.
[27] Y. Liu, I. Shin, I.-W. Hwang, S. Kim, J. Lee, M.-S. Yang, Y. K. Jung, J.-W. Jang, J. H. Jeong, S. H. Park, K. H. Kim, Single-Crystal-like Perovskite for High-Performance Solar Cells Using the Effective Merged Annealing Method, ACS Applied Materials & Interfaces 9 (2017) 12382–12390.
[28] C. Bi, Q. Wang, Y. Shao, Y. Yuan, Z. Xiao, J. Huang, Non-wetting surface-driven high-aspect-ratio crystalline grain growth for efficient hybrid perovskite solar cells, Nature Communications 6 (2015) ncomms8747.
[29] Y. Ma, P. M. Hangoma, W. I. Park, J.-H. Lim, Y. K. Jung, J. H. Jeong, S. H. Park, K. H. Kim, Controlled crystal facet of MAPbI3 perovskite for highly efficient and stable solar cell via nucleation modulation, Nanoscale 11 (2018) 170–177.
[30] M. Saliba, J.-P. Correa-Baena, C. M. Wolff, M. Stolterfoht, N. Phung, S. Albrecht, D. Neher, A. Abate, How to Make over 20% Efficient Perovskite Solar Cells in Regular (n–i–p) and Inverted (p–i–n) Architectures, Chemistry of Materials 30 (2018) 4193–4201.
[31] A. Fakharuddin, L. Schmidt-Mende, G. Garcia-Belmonte, R. Jose, I. Mora-Sero, Interfaces in Perovskite Solar Cells, Advanced Energy Materials 7 (2017) 1700623.
[32] S. Sun, T. Salim, N. Mathews, M. Duchamp, C. Boothroyd, G. Xing, T. Chien Sum, Y. Ming Lam, The origin of high efficiency in low-temperature solution-processable bilayer organometal halide hybrid solar cells, Energy & Environmental Science 7 (2014) 399–407.
[33] J.-Y. Jeng, Y.-F. Chiang, M.-H. Lee, S.-R. Peng, T.-F. Guo, P. Chen, T.-C. Wen, CH3NH3PbI3 Perovskite/Fullerene Planar-Heterojunction Hybrid Solar Cells, Advanced Materials 25 (2013) 3727–3732.
[34] J. C. Yu, J. A. Hong, E. D. Jung, D. B. Kim, S.-M. Baek, S. Lee, S. Cho, S. S. Park, K. J. Choi, M. H. Song, Highly efficient and stable inverted perovskite solar cell employing PEDOT:GO composite layer as a hole transport layer, Scientific Reports 8 (2018) 1070.
[35] C. Chen, S. Zhang, S. Wu, W. Zhang, H. Zhu, Z. Xiong, Y. Zhang, W. Chen, Effect of BCP buffer layer on eliminating charge accumulation for high performance of inverted perovskite solar cells, RSC Advances 7 (2017) 35819–35826.
[36] W. Shockley, H. J. Queisser, Detailed Balance Limit of Efficiency of p-n Junction Solar Cells, Journal of Applied Physics 32 (1961) 510–519.
[37] J. Nelson, The Physics of Solar Cells, World Scientific Publishing Company, 2003.
[38] S. Rühle, Tabulated values of the Shockley–Queisser limit for single junction solar cells, Solar Energy 130 (2016) 139–147.
[39] M. A. Green, Solar cells: Operating principles, technology, and system applications, Englewood Cliffs, NJ, Prentice-Hall, Inc., 1982. 288 p. (1982).
[40] Y. Kato, L. K. Ono, M. V. Lee, S. Wang, S. R. Raga, Y. Qi, Silver Iodide Formation in Methyl Ammonium Lead Iodide Perovskite Solar Cells with Silver Top Electrodes, Advanced Materials Interfaces 2 (2015) 1500195.
[41] C. Aranda, C. Cristobal, L. Shooshtari, C. Li, S. Huettner, A. Guerrero, Formation criteria of high efficiency perovskite solar cells under ambient conditions, Sustainable Energy & Fuels 1 (2017) 540–547.

Appendix

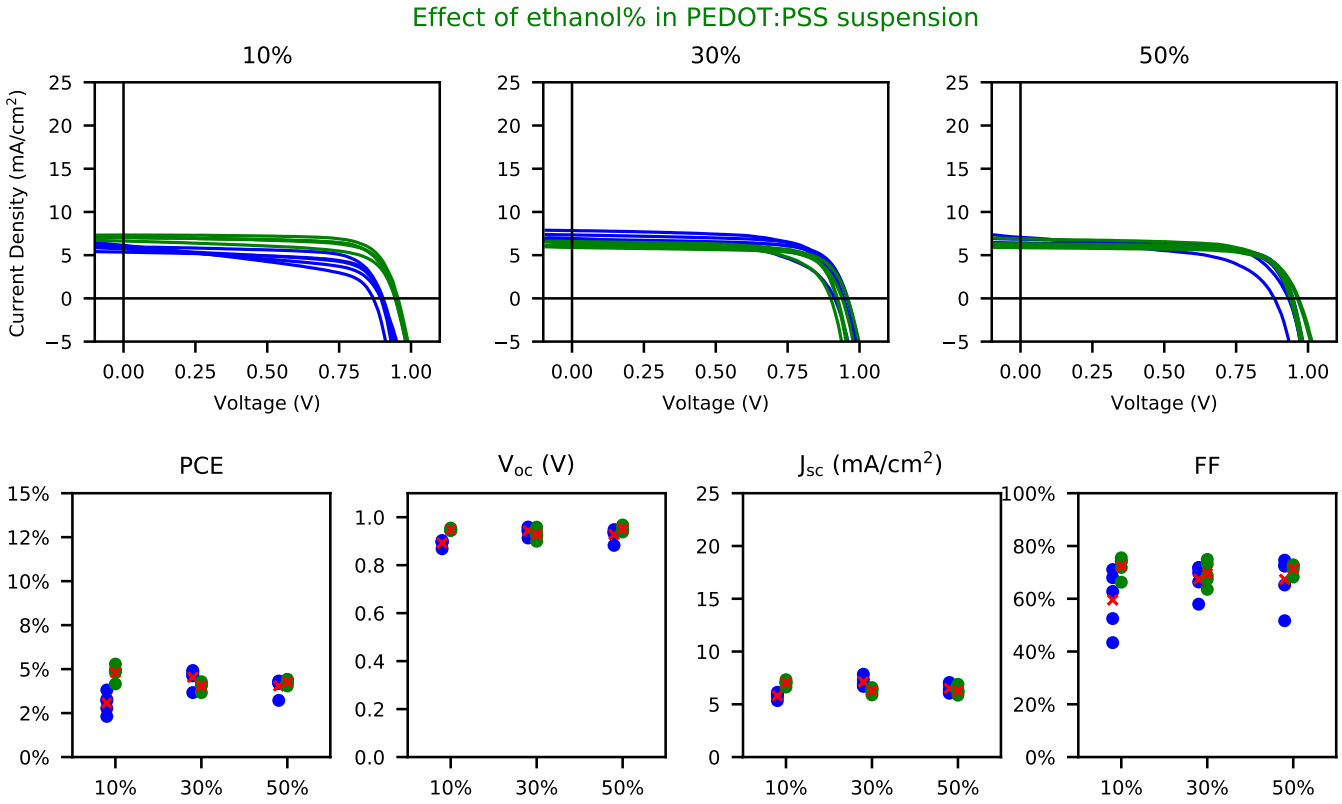

Figure A1: $MAPbI_3$ PSC fabricated with *Conventional Annealing* method under *Conditions A*. Experiment to determine the effect of varying the amount of ethanol in the PEDOT:PSS suspension. The ethanol greatly enhances the wettability and reduces the PEDOT:PSS thickness. The results show that it improves the reproducibility only. The mean values are almost identical in all parameters. Curves of the same color represent pixels of the same cell.

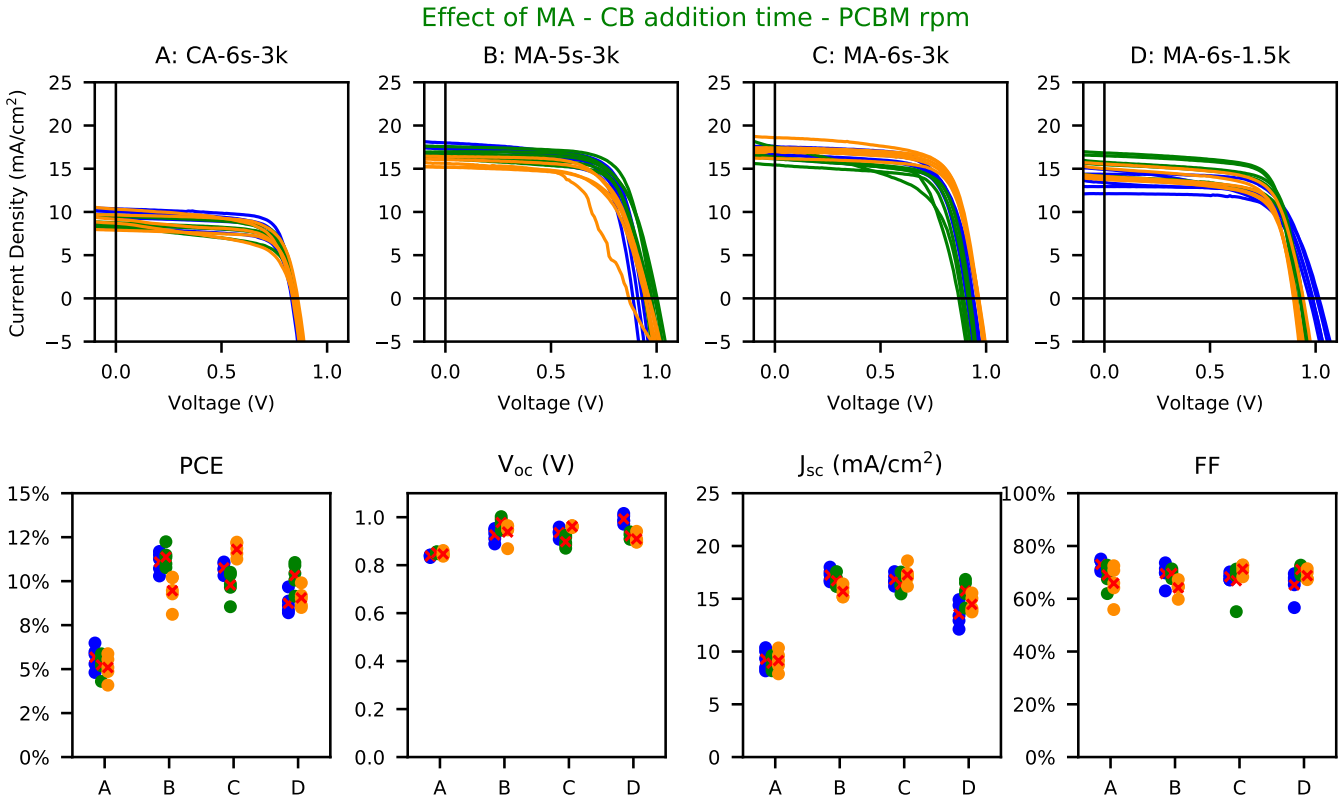

Figure A2: $MAPbI_3$ PSC fabricated under *Conditions A*. Experiment to determine the effect of using MA vs CA, the effect of adding the chlorobencene (CB) at the 5th second instead of the 6th second and the effect of depositing the PCBM at 1500 rpm (1.5k) instead of 3000 rpm (3k). The name code is: type of annealing - time of CB addition - PCBM rpm. Curves of the same color represent pixels of the same cell.

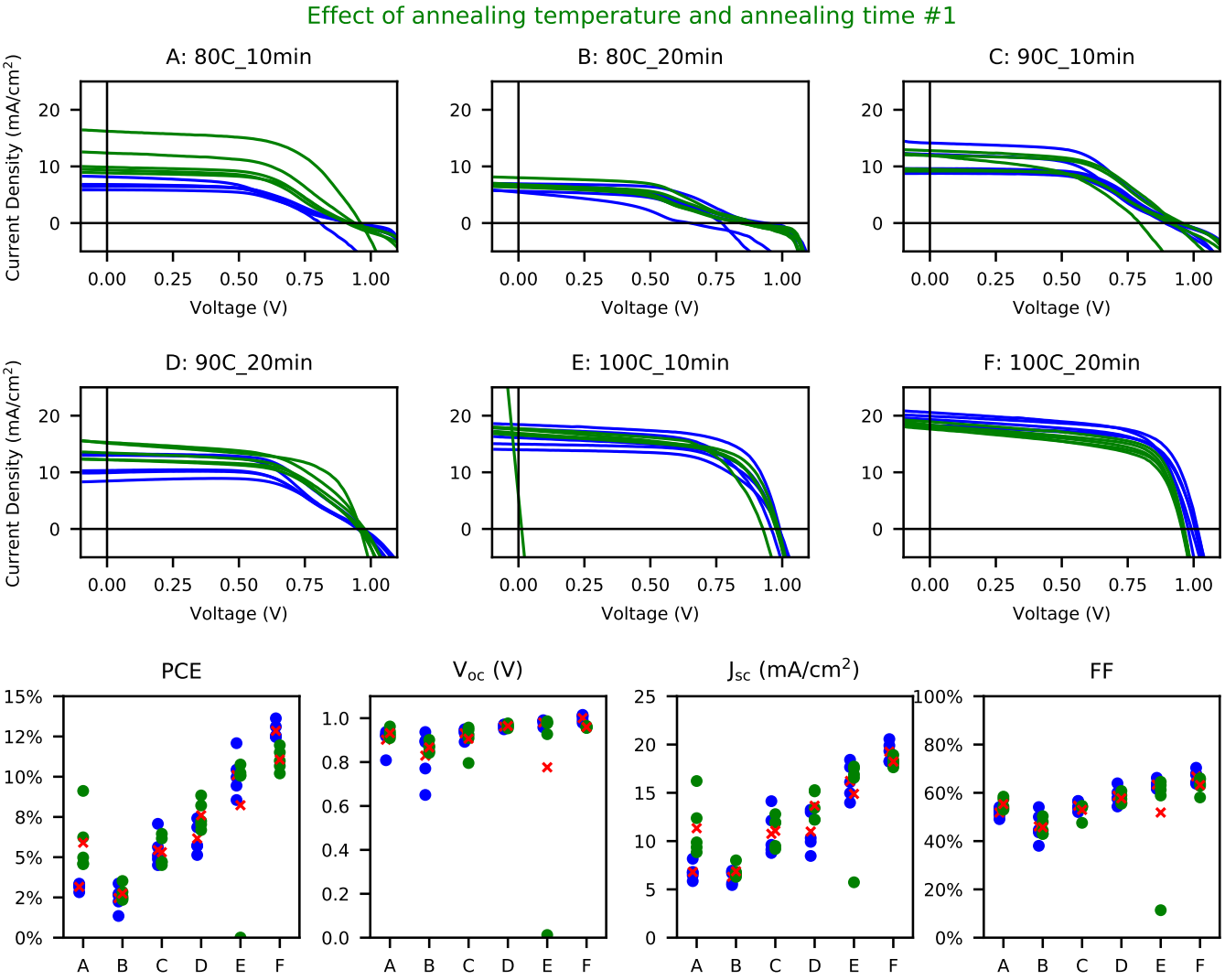

Figure A3: $MAPbI_3$ PSC fabricated under *Conditions A*. Experiment to determine the effect of annealing temperature and annealing time for the MA route. Curves of the same color represent pixels of the same cell.

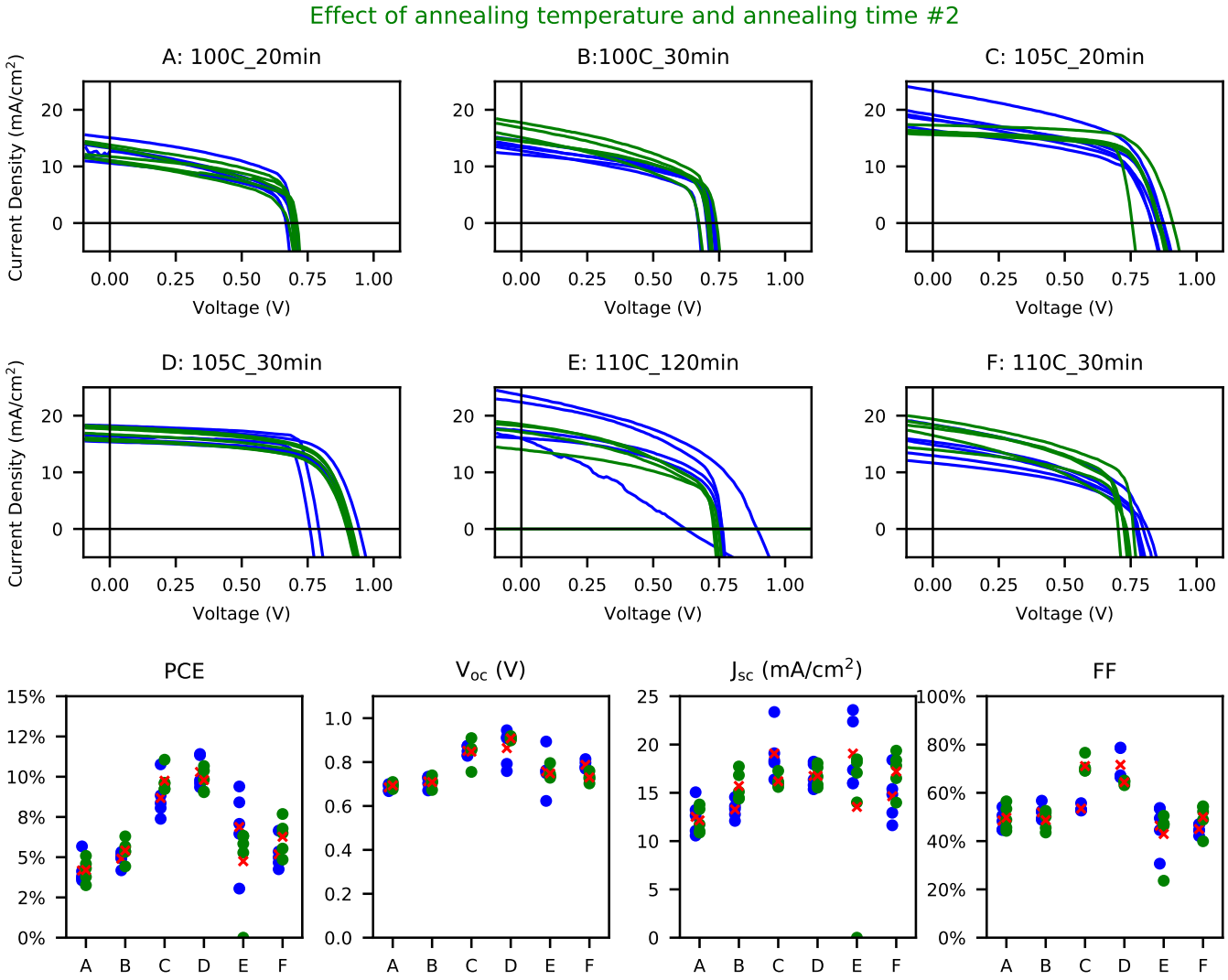

Figure A4: $MAPbI_3$ PSC fabricated under *Conditions A*. Another experiment to determine the effect of annealing temperature and annealing time for the MA route. The only difference with Fig. A3 was that the PCBM solution was heated to 60°C instead of 40°C. Curves of the same color represent pixels of the same cell.

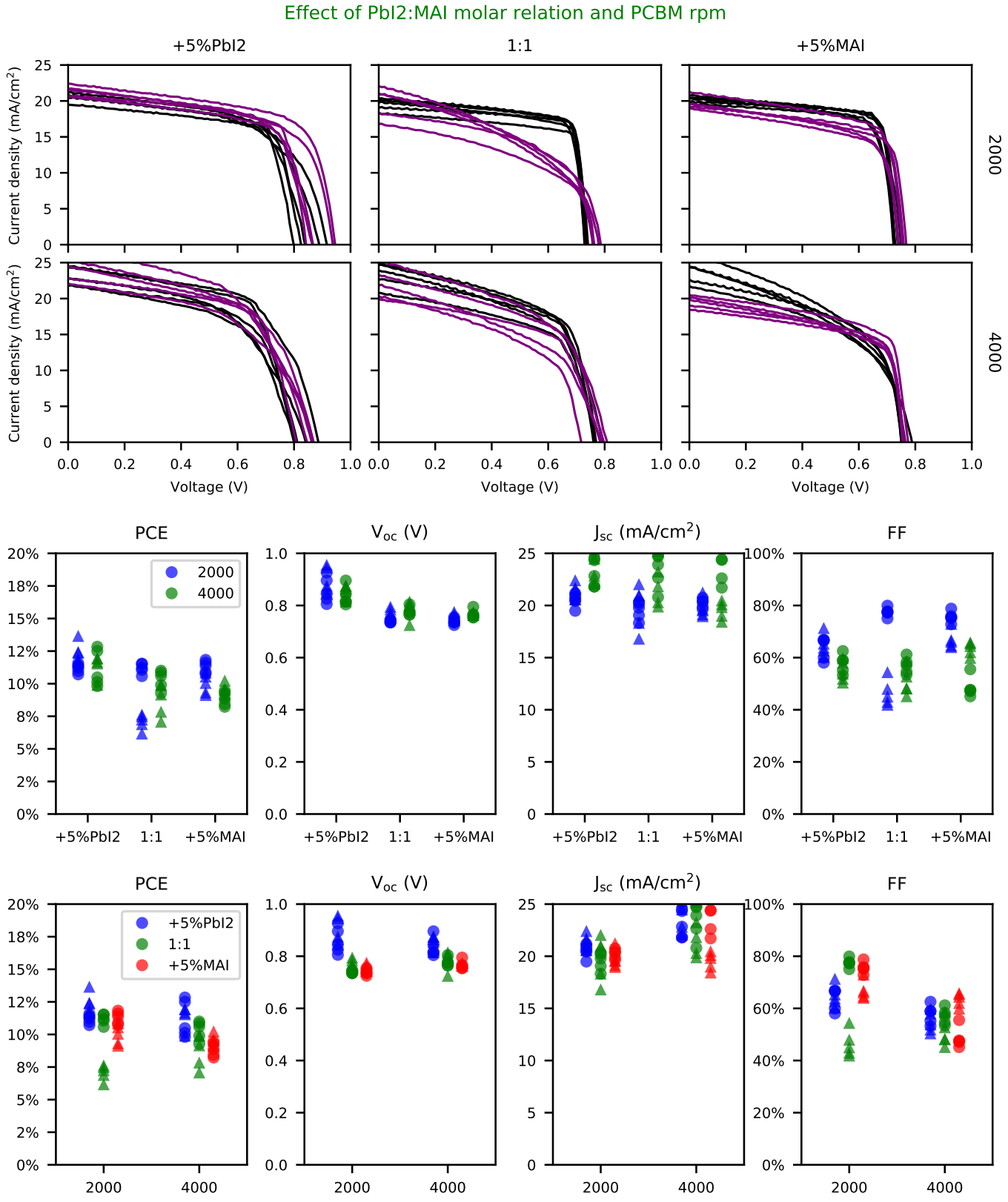

Figure A5: $MAPbI_3$ PSC fabricated under *Conditions A*. Factorial study of the effects of the molar relation between PbI_2 and MAI and the PCBM deposition speed for the MA route. Curves of the same color represent pixels of the same cell.

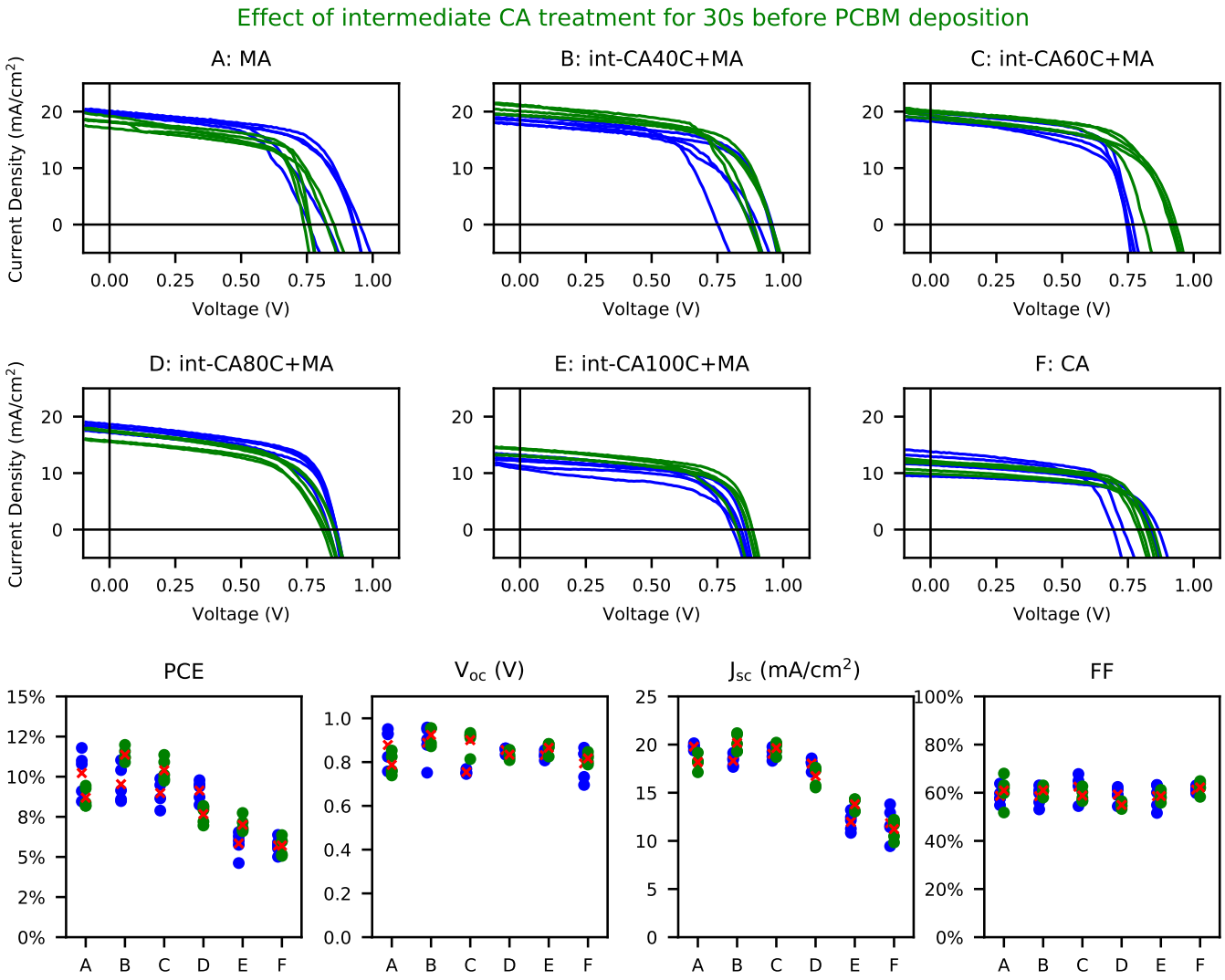

Figure A6: $MAPbI_3$ PSC fabricated under *Conditions A*. Study of the effect of preheating the perovskite for 30s at a given temperature before covering with PCBM for MA. The higher the temperature, the darker the films before PCBM. The films were Annealed at 105°C for 30 min. Curves of the same color represent pixels of the same cell.

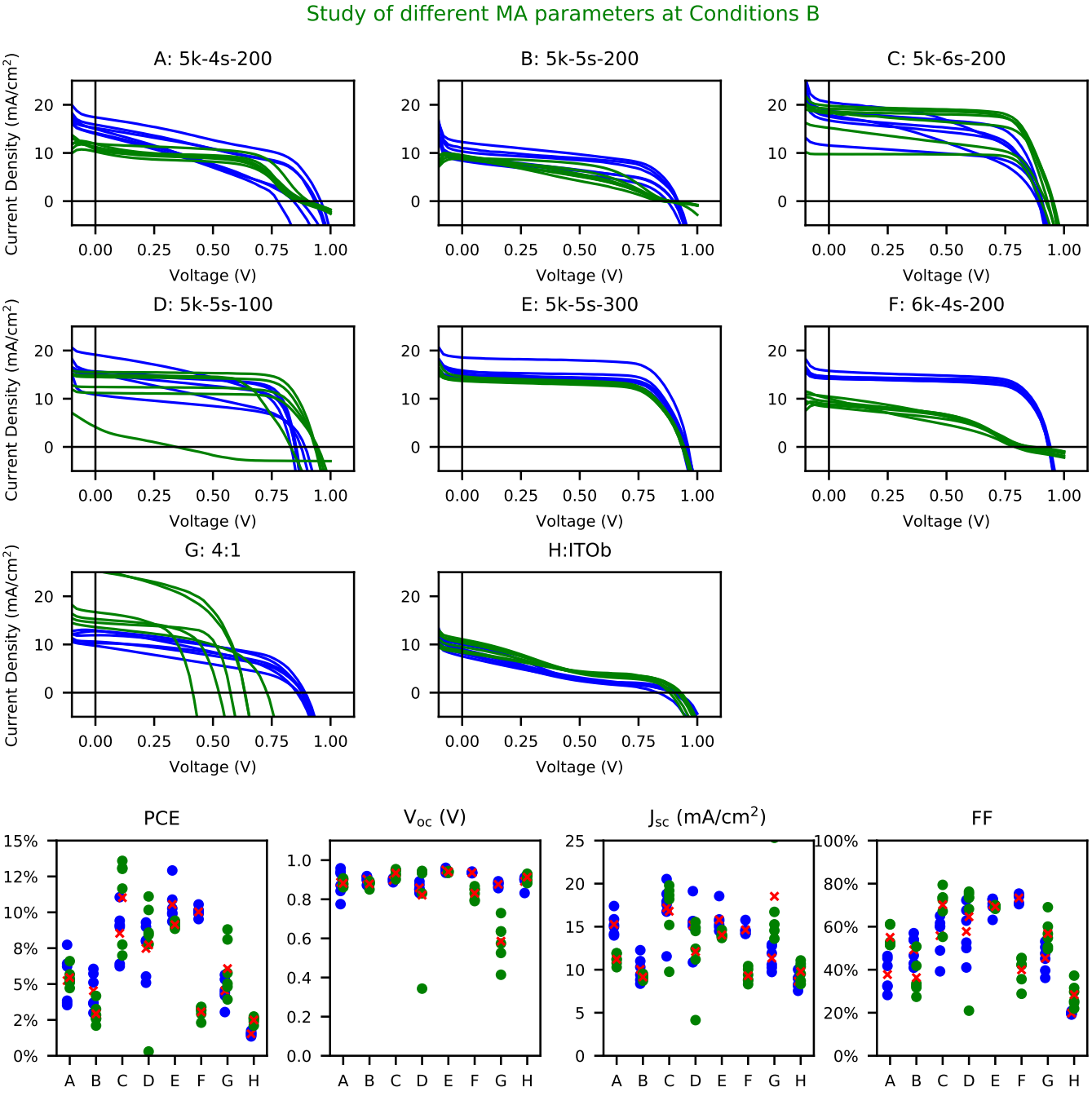

Figure A7: $MAPbI_3$ PSC fabricated under *Conditions B*. Experiment to determine several effects of changing MA parameters: 5000 vs 6000 rpm for perovskite rpm, 5s vs 6s CB addition, 100 vs 200 vs 300 uL of CB for quenching. The name code is: perovskite rpm - time of CB addition - vol. of CB except for figures G and H. G was made with a 1:4 DMSO to DMF ratio, and H is exactly like B but with another brand of ITO glass. Curves of the same color represent pixels of the same cell.

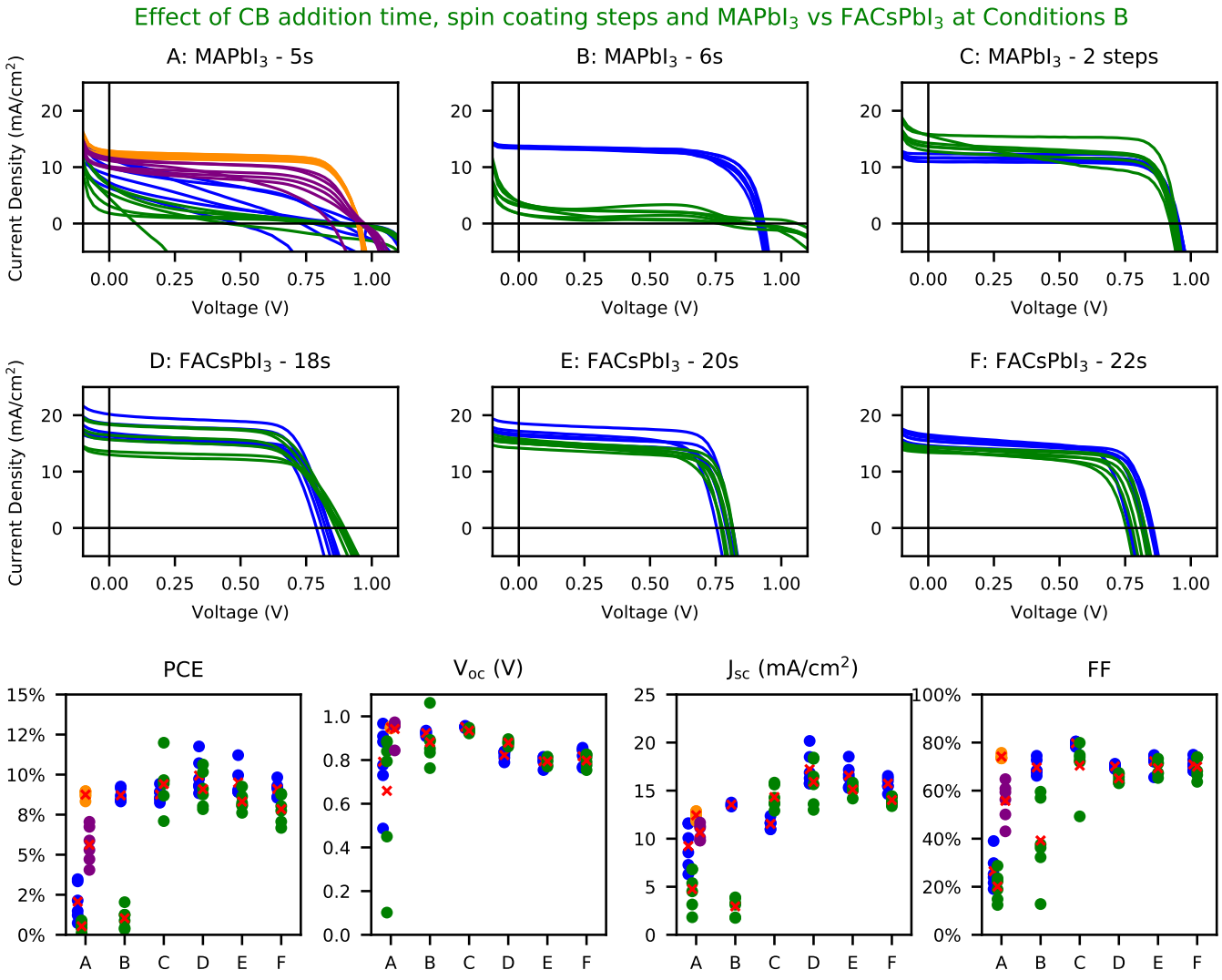

Figure A8: $MAPbI_3$ and $FACsPbI_3$ PSC fabricated under *Conditions B*. Experiment to establish the effect of CB addition time. Also an experiment was performed for $MAPbI_3$ with a 2 steps spin coating program, 10s at 1000 rpm and then 10s at 5000 rpm in graph C. Curves of the same color represent pixels of the same cell.

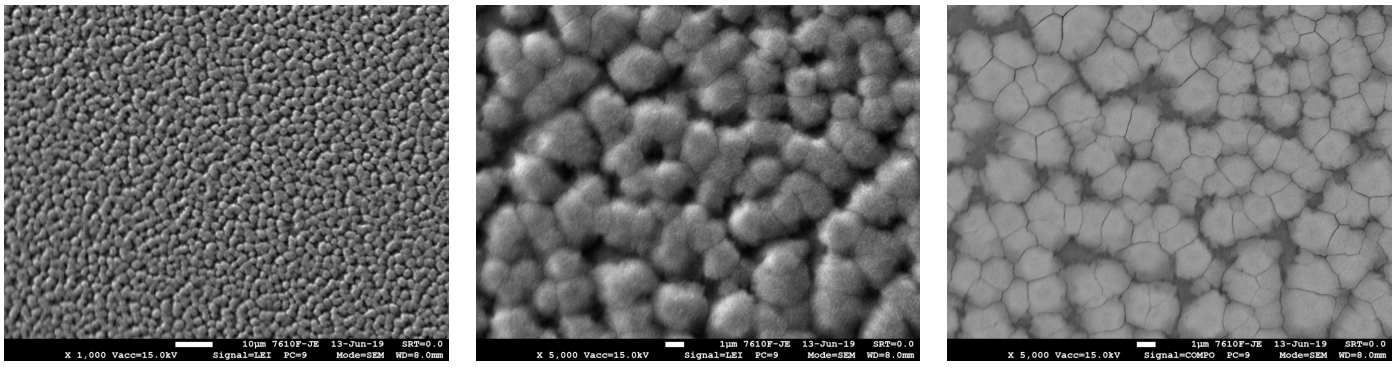

(a) (b) (c)

Figure A9: SEM frontal images of $MAPbI_3$ perovskites deposited using MA with a DMF to DMSO ratio of 4:1. (a) and (b) were measured with a low energy electrons detector and (c) with a back-scattered electrons detector. The scale-bar in (a) is for 10 µm and in (b) and (c) is for 1 µm

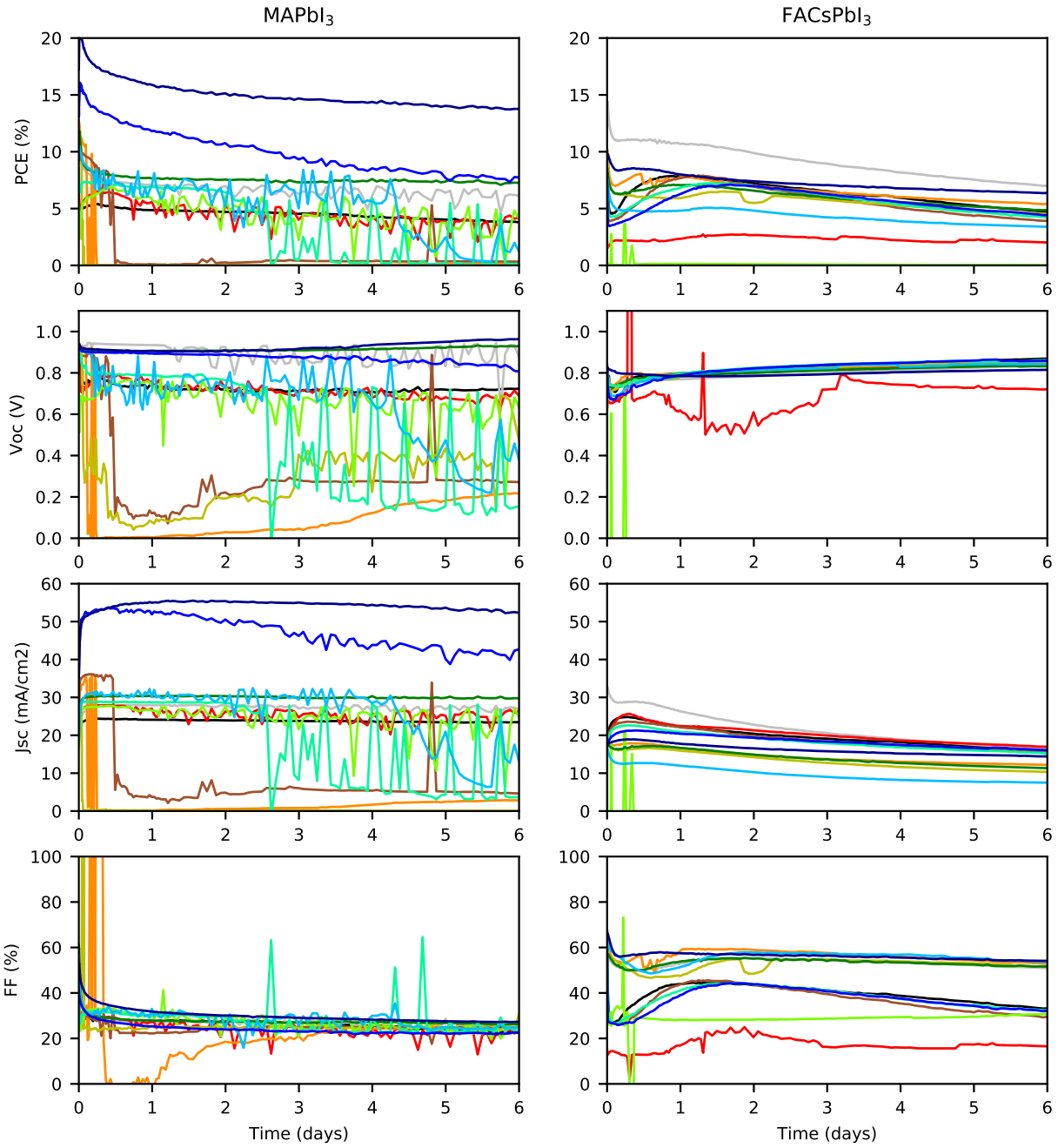

Figure A10: Stability study for the different perovskites under constant 1 sun illumination and inert atmosphere. The values are normalized to the initial value. The value of efficiency is inaccurate because the LED system used for the experiment was not exactly calibrated for 1 sun.